Benemérita Universidad Autónoma de Puebla

Facultad de Ciencias Físico Matemáticas

Charge studies on Multigap Resistive Plate Chambers

Master Thesis in Experimental Physics

Author:
Manuel Alejandro Del Rio Viera

Mentor:
Dra. Cecilia Uribe Estrada

Dr. Gerardo Francisco Torres Del Castillo

June 2020

Abstract

With demands for more precision both in HEP (High Energy Physics) and in industry, there is considerable research and development concerning precise time and position measurements from a variety of detectors.

Resistive Plate Chambers (RPCs) are fast gaseous detectors with high spatial and temporal resolution. They were conceived in 1981 and used to detect charged particles in HEP. Multigap Resistive Plate Chambers (MRPCs) were introduced later to improve the time resolution and they have been used as time-of-flight (TOF) detectors both in HEP and in medicine (PET) .

RPCs consist of two parallel plates, a positively-charged anode and a negatively-charged cathode, both made of a very high resistivity material and separated by a gas volume. When a charged particle enters the gas gap it can ionize the gas molecules to create electron-ion pairs.

Due to the electric field, the ions travel towards the cathode and the electrons towards the anode, inducing signals on the pickup electrodes. The moving electrons are also subject to an avalanche process, which amplifies the signals. Ultimately, the acquired data provides information such as time-of-flight and position telling us where and when an event occurred. The higher pile-up (interactions per crossing) of future colliders, such as the High Luminosity Large Hadron Collider (HL-LHC), will present new challenges for tracking. Higher time resolution (on the order of a few tens of picoseconds), when added to spatial information, will permit 4-D tracking even in quite harsh environments.

The main goal of our R&D is to design and build MRPCs to improve their measurement capabilities. In this project the main task is to measure the total charge deposited in a 20 gap MRPC with 2 different gap sizes, which is a critical factor for a high rate environment.

Acknowledgements

I wish to thank all the people whose assistance in the completion of this project was crucial. I want to thank my mentor Cecilia Uribe Estrada for her patience and affording me many opportunities. I consider meeting Crispin Williams an accomplishment by itself and I'm truly grateful for him providing his time and support. Roman Zuyeuski and Zheng Liu were such nice persons to work with and learn from and I'm thankful to them allowing me in their space to work with their creations. Yongwook Baek , Jinsook Kim and Byeongguk Min were very kind, supportive and always there. Thank you so much to all.

To my beloved parents.

Contents

1 Introduction **9**
- 1.1 Brief History of Gaseous Detector Designs . . . 10
- 1.2 The vast importance of detectors . . . 12
- 1.3 How to use this thesis . . . 13

2 Fundamentals of the Resistive Plate Chambers **15**
- 2.1 Design . . . 15
- 2.2 Physics of the RPC . . . 17
  - 2.2.1 Avalanche Formation . . . 17
  - 2.2.2 Cluster Size . . . 18
  - 2.2.3 Signal Formation . . . 19
  - 2.2.4 Total and Fast Induced Charge . . . 20
  - 2.2.5 Efficiency . . . 20
  - 2.2.6 Diffusion . . . 21
  - 2.2.7 Electrical Field Strength . . . 22
  - 2.2.8 Ramo's Theorem . . . 23
  - 2.2.9 Space Charge . . . 27
- 2.3 Streamer and Avalanche Mode . . . 29

3 Experimental Setup **31**
- 3.1 MRPC Construction . . . 31
- 3.2 Setup . . . 33

4 Experimental Results **37**
- 4.1 Measurement of the Signal . . . 37
- 4.2 Measurement of the Capacitance . . . 39
- 4.3 Analysis Procedure . . . 41
- 4.4 Charge Distribution . . . 42
- 4.5 Fast Charge to Total Ratio . . . 43
- 4.6 Total Charge . . . 45
- 4.7 Fast Charge . . . 46
- 4.8 Streamers . . . 47

5 Parameters for the Simulation of the MRPC **51**
- 5.1 Voltage and Electrical Field Distribution Inside the Gas Gap . . . 51
  - 5.1.1 Voltage Distribution . . . 51
  - 5.1.2 Electrical field Distribution . . . 52
- 5.2 Cluster Density . . . 54
- 5.3 Energy deposited . . . 55
- 5.4 Townsend and Attachment Coefficient . . . 56
- 5.5 Drift Velocity . . . 59

5.6 Diffusion 60

6 Description of the MRPC Simulation **61**
6.1 Simulation Algorithm 62
6.2 Limitations of the Simulation 62

7 Simulation Results **63**

8 Conclusions **69**

9 Bibliography **71**

Chapter 1

Introduction

Human nature has always pushed its curiosity to try to understand its surroundings, from the vast space we live in and the celestial bodies which populate it to the minuscule elemental parts that constitute matter. The need to explain nearly everything has always been accompanied with the creation of new ways to treat unknowns that result in different means of understanding our world. This inventive process could be as simple as arranging one's surroundings in a certain way or extremely complicated such as the development of new technology that lets us interact with our surroundings. The latter occurs more often than not for phenomena that are far out our reach, such as at cosmic and microscopic ranges.

It is of special interest for us to discuss the microscopic realm as it concerns our area of investigation for this paper. In order to be able to interact with this domain, the use of various devices is required. Many of these devices allow us to interact in various manners with different phenomena that are confined to the experiment of interest. Some of the most important of these devices are detectors. A detector is a device that allows one to perceive a certain event, which can be achieved by various methods depending on the desired detection, such as the detection of gas from a leak in a tank, or the presence of smoke indicating a fire. Our topic of interest is the microscopic realm, particularly the detection of cosmic charged particles and how these charges affect the functioning of a specific detector, the Resistive Plate Chamber (RPC). This detector is capable of tracking charged particles that enter its gap filled with gas, producing ionization which induces a retrievable signal. As the signal is the final result of the detection process and of vital importance for the good functioning of the chamber, we will discuss how the signal develops and the effects of the charge processes that are involved for two chambers which, although similar, present meaningful differences that affect the amount of average charge deposited by the avalanche process and its implications.

1.1 Brief History of Gaseous Detector Designs

All gaseous particle detectors operate under the principle of ionization. As a particle passes through the gas volume it ionizes the gas, causing free charged particles to move towards the electrodes due to an electrical field applied to this gas volume. The movement of these charged particles produces induction that can be retrieved as a signal by the surrounding electrodes. Note, however, that the process of charge multiplication differs heavily from design to design.

This ionization mechanism has been used as early as the 1900's with the creation of the first **ionization chambers**. Such detectors had cylindrical geometry with two metallic electrodes: a central wire serving as an anode and a cathode surrounding it. A voltage is applied between the anode and cathode and the gap volume is filled with gas.

Depending on the necessities of the experiment the geometry of these chambers could vary between cylindrical, planar or even spherical. Although the principle of operation does not depend on the geometry, it can affect properties such as the distribution of the electrical field inside the chamber.

The electrical field in a cylindrical geometry gets stronger as it reaches the central wire, resulting in a small region were the field is strong enough to achieve an electron avalanche. However, due to a very small multiplication region -in part related to this design- a limited time resolution is obtained. When an ionizing particle passes through the gas volume, the electrons formed drift from the lower field region to a small region with an electrical field high enough to produce an avalanche, making this an slow process. For this reason, the planar geometry, often called the **Parallel Plate Ionization Chamber**, was later introduced.

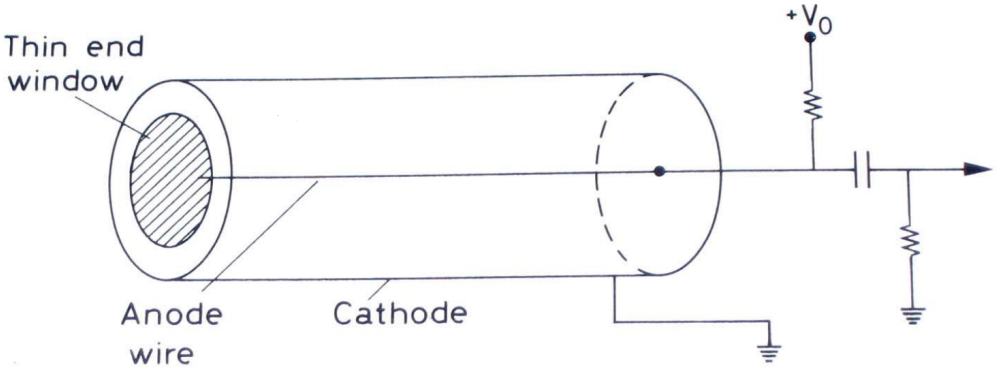

Figure 1.1: Scheme of an ionization chamber

One of the first detectors using this advantageous design is the so-called **Parallel Plate Counter (PPC)** developed by J. W. Keuffel in 1948. The first prototypes consisted of two molybdenum disks, replaced later by copper, separated by a 3.0 mm gap. The units were flooded with a gas mixture of xylene vapors at a pressure of 0.5 atm and a voltage of 1 to 3 kV was applied. The parallel plate geometry allows for a uniform field between the electrodes. If the applied electric field is strong enough, all of the volume becomes active, which means that an ionizing particle could trigger a spark in all of its volume.

However, this design proved to have many flaws. After the passage of an ionizing particle, due to the plates being made of a conductive material a continuous discharge occurred -fed by charge of these conductive electrodes- so an external switch was necessary to shut down the applied voltage from .01 up to .05 seconds. This happened to be a major problem particularly when trying to retrieve arrival times or operating at higher particle rates.

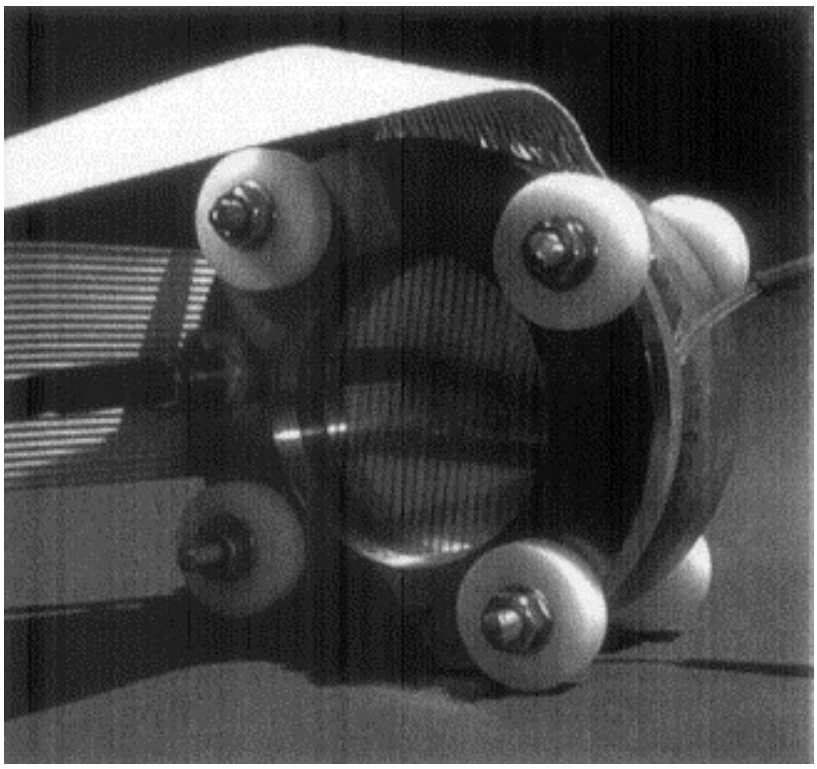

Figure 1.2: A Parallel Plate Counter **[1].**

Nevertheless, although delicate and difficult to construct and operate, this was a first approach to a new wave of detectors whose flaws were gradually minimized over the years while their design was similarly improved. The most important change arrived in 1964 with the development of the Parallel Plate Avalanche Counter which utilized the avalanche mode, applying a low continuous voltage not reaching the **Raether limit [2]**, avoiding the transition to streamers. This allowed one to operate continuously and at higher rates than the spark chambers. The electrodes implemented were metallic and often solid but sometimes in the form of meshes.

The **Resistive Plate Chamber (RPC)** was developed in early 1980 by Rinaldo Santonico and Roberto Cardarelli as a fast and economic detector, that was able to use the advantages of both planar geometry and the use of resistive electrodes, but also make them easier to build in order to cover large surfaces. The chosen material for the first RPC electrodes of this kind was Bakelite, a high pressure laminate (HPL) that can be adapted to requirements with the use of heat, pressure or chemicals.

The basis for this is the Parallel Plate Counter, a planar geometry that allows for a homogeneous electrical field across a gap filled with gas. Particles that enter this gap ionize the gas, producing a signal.

Variants of detectors of this kind have been used in many experiments around the world due to their relative low cost, excellent time resolution and their simple construction and operation.

1.2 The vast importance of detectors

Particle physics is the branch of physics that concerns the nature of the particles that constitute matter and radiation. Ever since the development of particle physics, the need for particle detection has been fundamental. From the discovery of the electron in 1897 by Sir Joseph John Thomson to the Higgs Boson in 2012, particle detectors had been available to allow us to observe various phenomena ranging from the simplest to the most complicated mechanisms. As the requirements for greater accuracy, efficiency, or sensitivity increased, so did the complexity of the detectors and their operation.

The detection of particles is not only useful for particle physics but many other areas as well. For instance, dosimeters are used to retrieve information on the amount of radiation in the environment. Such information is useful when considering safety around radiation sources, or for medical purposes where linear accelerators are used. Furthermore, the ability to reconstruct images in Positron Emission Tomography (PET) is possible with the detection of photons emitted via pair annihilation. Even X-ray film is considered a simple detector: the film turns black as it is hit by radiation but remains translucent where the rays are blocked, such as by bones.

Expanding on the use of detectors for safety purposes, the smoke detector, a staple since its patent in 1890, uses a detector system coupled with an alarm in order to detect the presence of smoke, to infer the existence of a fire source. Detection of radiation sources within buildings in order to take out hazardous materials is also widespread. Gas detection allows one to avoid gas leaks that could lead to gas poisoning or explosions. The list goes on and on.

1.3 How to use this thesis

The information summarized in this thesis is the learning accumulated over a year stay at CERN. Although filtered through my personal point of view, the information gathered here owes its provenance to one of the most recognized and influential people in the subject.

Each chapter in this work focuses on a fundamental topic of Resistive Plate Chambers:

- Chapter 2 covers some of the basic physical processes that the RPC involves, from avalanche multiplication to space charge effects.
- Chapter 3 explains the construction and setup of our experiment, which besides the construction of the chambers themselves and the equipment, is very accessible due to the lack of complicated output and amplification electronics.
- Chapter 4 discusses the experimental results that were retrieved. We analyze these and try to explain their behaviour, discrepancy or accordance with the known models.
- Chapter 5 shows some important parameters that have to do with the processes inside every gaseous detector.
- Chapter 6 describes briefly the ideas behind the simulation of the detectors and their problems or limitations.
- Chapter 7 compares some of the previous results and detector designs and tries to hopefully replicate the behaviour of said results.
- Chapter 8 contains the conclusions of the results of this thesis.

Chapter 2

Fundamentals of the Resistive Plate Chambers

2.1 Design

The basic idea of the Resistive Plate Chamber is that of a parallel plate capacitor. This consists of two parallel resistive plates of a certain thickness separated by a gas-filled gap, which can span a range from micrometers to a few millimeters. A DC voltage is applied to the electrodes by a layer of graphite paint on their inner surface. In the outer part of the electrodes the pick up strips or pads are placed. These collect the signal produced by the movement of charged particles created along the ionizing path of particles that enter the gap.

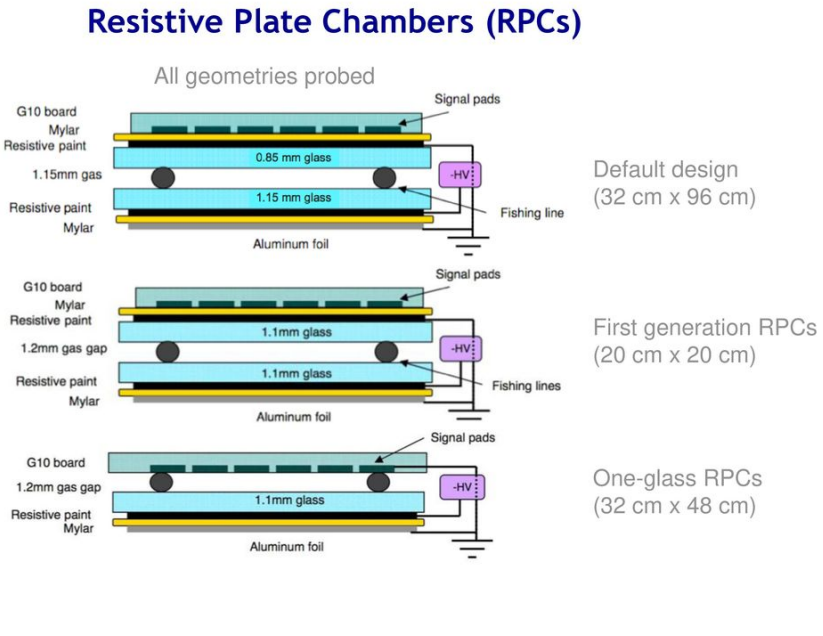

Figure 2.1: Example of RPC designs [**3**].

The resistive material of the electrodes can vary depending of the necessities of the detector, with the most common being Bakelite and glass. The electrode material often denotes the name of the RPC, such as "Glass RPC" or "Bakelite RPC". In this paper we will focus on the glass variant of the RPC. However, when pertinent we will mention some of the differences between these materials.

While an RPC denotes a single gap configuration, a **Multigap Resistive Plate Chamber (MRPC)** denotes, as the name implies, a multiple gap configuration. The way to achieve this is by placing resistive materials to separate an existing gap. These new plates will function as electrodes, electrically floating, with each gap working exactly as an RPC on its own. Fishing line is used as a spacer for smaller gaps required in the construction of an MRPC. Depending on the size of the desired gap, the thickness of the fishing line can be chosen accordingly.

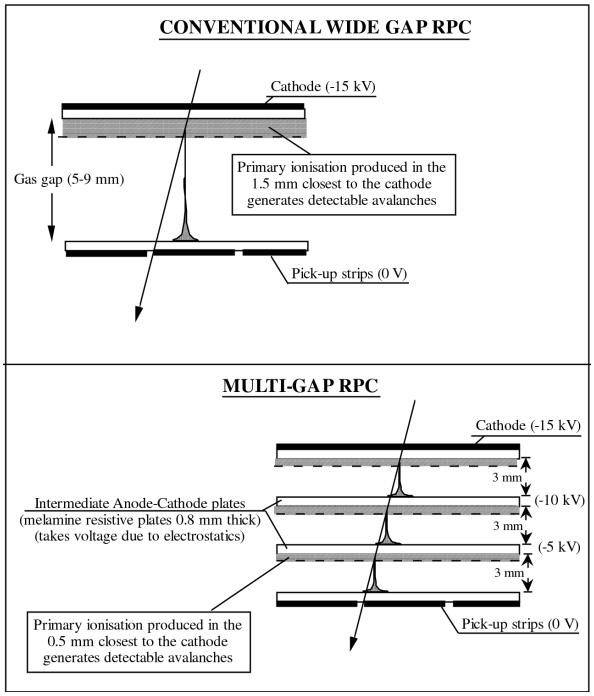

Figure 2.2: Example of both RPC and MRPC designs.

The voltage applied distributes differently depending on the configuration. While for a single gap the effective voltage would end up being the same as the one applied into the gap, the case for the multigap differs. For the multigap configuration the voltage is divided in function of the number of gaps, reducing the voltage for each gap but keeping the effective voltage the same.

The main problem with a multigap design is that it is a much more complicated process to construct compared to a regular single gap configuration, nevertheless this design has many advantages such as the reduction of the operating voltage without reducing the total signal achieved. This occurs due to the reduction of the width of the gas gap causing an increase in the effective electric field applied. However, the overall effective width of the chamber, being the sum of all the gaps in the multigap configuration, is not affected.

2.2 Physics of the RPC

Although simple in design, the physical processes involved within the Resistive Plate Chambers are complex compared to other gaseous detectors. In this section we will go through the basic physical principles of operation that concern this kind of detector.

2.2.1 Avalanche Formation

The narrowness of the gap allows for a homogeneous and strong electrical field across the gap. When a particle enters the gap, in particular, a charged particle, it can experience various phenomena that include elastic and inelastic collisions. In elastic collisions, the particle does not lose kinetic energy, but instead due to the powerful electrical field, it can increase as:

$$E_k = |q|\Delta V \tag{2.1}$$

where q is the particle charge and ΔV is the voltage difference in the zone that the particle is traversing.

In an inelastic collision the particle loses energy and can excite the atoms or molecules at different levels. The most important of these processes is ionization, where an electron is freed into the gas volume and produces an ion-electron pair.

The increase of the number of free electrons, n_e, in the gas volume with respect to the distance is given by:

$$\frac{dn_e}{dx} = \alpha n_e \tag{2.2}$$

where α is the first Townsend coefficient, which represents the probability for an electron to generate additional ion-electron pairs per unit length and has a dependence on the electrical field. This coefficient has the following form:

$$\alpha = Ape^{-\frac{Bp}{E}} \tag{2.3}$$

where A and B are constants, p is the gas pressure and E the electrical field.

Under the assumption that the electrical field is homogeneous across the gap and the gas pressure is constant, the dependence on gas number density, n_A, i.e. the number of gas atoms or molecules per cubic meter, can be neglected.

If we integrate this expression we obtain:

$$n_e = n_0 e^{\alpha d} \tag{2.4}$$

This is called the Townsend equation, where n_0 is the number of primary electrons. The term $e^{\alpha d}$ is called the gas gain and d is the distance where the bunch of ion-electron pairs appear, a so-called avalanche, that in the case of a parallel geometry tends to be the width of the gap. This statement will be explained later when we treat signal formation.

Due to the difference in mass between the drifted electron and positive ions, their velocity will also differ. The electron avalanche starts with the electrons produced along the path of the ionizing particle. Due to the high electrical field across the gas gap (achieving a high gas gain), a single electron produces two, two produces four and so on. Along with the production of an electron, a positive ion is also formed, creating two distinctive parts of the electron avalanche:

- a fast "head" moving towards the anode, created by energetic electrons; and
- a conical-shaped "body"consisting in positive ions slowly drifting in the opposite direction.

The time that the electrons take to reach the anode -for an electrical field in the range of 50-100 kV/cm- is of the order of a few nanoseconds; while the positive ions require a few microseconds to reach the cathode [**4**].

In summary, the RPC takes advantage of the gas multiplication (or gas gain) of the ions and electrons, due to the ionization path of a charged particle that passes through the gap. This primary ionization event causes clusters of electrons (and positive ions) along its path that behaves like a Poisson distribution. Due to the high electrical field the electrons and positive ions then proceed to drift in opposite directions towards the electrodes. This can cause even more ionization as expressed in **equation 2.4**. At last, this movement induces a charge in the pick up electrodes creating a signal.

2.2.2 Cluster Size

Let us start by considering a single gap RPC whose gas gap has been traversed by an ionizing particle producing n_{cl} clusters along its path. This value is dependent on the energy of the primary ionizing particle, the gas mixture and the gap width. Let us define the cluster density as $\lambda_{eff} = \frac{\lambda}{cos\phi}$ where λ is the number of clusters per millimeter and ϕ the incident angle between the path of the particle and the electrodes. Assuming that the energy lost by the particle is negligible compared to its total kinetic energy, so that the cluster density remains constant over the gap, the probability P_{cl} that n_{cl} clusters are created in the gas gap (with a width of d) is:

$$P_{cl}(n_{cl}) = \frac{(d\lambda_{eff})^{n_{cl}}}{n_{cl}!} e^{-d\lambda_{eff}} \tag{2.5}$$

Due to its nature, a Poisson distribution follows and as expected the mean value of the number of clusters produced is just $d\lambda_{eff}$, i.e. the product of the cluster density and the gap width. This number also depends on the gas mixture and the energy of the ionizing particle entering the gap.

With this in mind, we can also study the cluster spatial distribution along the gap. Denoting the initial position of the j-th cluster by x_0^j. These values also follow a Poisson distribution given by:

$$P_{cl}(x_0^j = x) = \frac{j\lambda_{eff}}{(j-1)!} (x\lambda_{eff})^{j-1} e^{-x\lambda_{eff}} \tag{2.6}$$

where $0 < x < d$ and $x = 0$ corresponds to the position of one of the electrodes [**4**].

2.2.3 Signal Formation

As charge moves towards (or away from) the electrodes, a signal is induced in the pick up readout. The amount of induced current produced by these moving charges is given by **Ramo's theorem**:

$$i_{ind}(t) = qN(t)\boldsymbol{\nu_d} \cdot \boldsymbol{E_w(x(t))} \tag{2.7}$$

where q is the charge of the particle, N is the number of particles in the cluster, $\boldsymbol{\nu_d}$ their drift velocity and $\boldsymbol{E_w}$ is the **weighting field** at the position x at the time t. The weighting field is a consequence of the weighting potential and is not a measurable quantity, unlike the electrical field.

The total amount of charge is the sum of all the induced currents over all of the clusters which have been formed, i.e. the avalanche. The drift velocity of the electrons during avalanche formation is higher than that of the ions due to their mass differences, meaning that current induction for the ions is smaller compared to the faster electrons.

The induced charge is simply the integral over the total induced current:

$$q_{ind}(t) = \sum_{j=0}^{n_{cl}} \int_{t_0}^{t} qN(t)\nu_d E_w(x(t))dt \tag{2.8}$$

where the sum is over all of the clusters formed during the avalanche.

Due to the use of high resistive materials as electrodes, the avalanche is confined to a small volume, not affecting nearby regions. The presence of these charges affects the electrical field inside the gaps, but as the charges reach the electrodes the signal terminates. However, these charges are eventually absorbed by the electrodes and the field returns to its original value. This is called the **relaxation time**. This value has been found to be:

$$\tau = 2\rho_r\varepsilon_0(2\varepsilon_r + \frac{d}{g}) \tag{2.9}$$

where ρ_r is the bulk resitivity of the electrode, ϵ_0 the vacuum permitivity, ϵ_r its relative permitivity, d its width and g the gap width. The area affected by the avalanche can be calculated as:

$$S = \frac{\bar{Q}}{\varepsilon_0 E} \tag{2.10}$$

where $\bar{Q}$ is the mean charge generated during the avalanche and E the magnitude of applied electrical field [**5**].

2.2.4 Total and Fast Induced Charge

The induced charge is due to the charged moving particles inside the gap. Two main charge sources can be distinguished: electrons and positive ions. The total induced charge is the total amount of charge induced by these two main sources, while the fast induced charge is the one induced just by the electrons. The drift velocity of the latter, as we stated before, is much higher, explaining the origin of the term "fast".

Unlike the induced current, the fast charge tends to be negligible compared to the total due to the fact that as the avalanche grows, the electron avalanche reaches its maximum density at the anode, thus drifting less distance compared to the positive ions, that drift over the whole gap . Furthermore, with the condition that the gas gain is much greater than one, something which happens at very high electrical fields (around the 100 kV/cm), the ratio between the fast to total induced charge reduces to:

$$\frac{q_{fast}}{q_{total}} \approx \frac{1}{\alpha d} \tag{2.11}$$

This last relationship presents a decreasing behaviour as the gas gain increases. For example, for $\alpha d = 14$ a gas gain of 10^6 is obtained and the ratio is around 7% , while for αd=18.42 a gas gain at the **Raether limit** $\sim 10^8$ is obtained and a ratio of 5% is obtained.

2.2.5 Efficiency

In order for an RPC to be efficient, it has to be able to produce a detectable signal. The biggest signals are produced by electron-ion pairs created near the cathode that allow for the electrons to avalanche the full width of the gas gap.

The efficiency of a single gap is related to the average number of clusters created within:

$$\epsilon = 1 - e^{-\lambda_{eff} d} \tag{2.12}$$

Assuming n independent gaps as well as denoting the efficiency of a single gap as ϵ_{gap}, the efficiency of the total is:

$$\epsilon_{tot} = 1 - (1 - \epsilon_{gap})^n \tag{2.13}$$

This is due to the fact that the probability of every single gap being inefficient is:

$$(1 - \epsilon_{tot}) = (1 - \epsilon_{gap})^n \tag{2.14}$$

and that the efficiency is just the complement of the inefficiency.

2.2.6 Diffusion

The energy distribution of a free electron cloud in a gas follows a Maxwell-Boltzmann distribution, with a mean defined by the thermal energy of the cloud:

$$< E >= \frac{3}{2}kT \tag{2.15}$$

with k the Boltzmann constant and T the temperature of the gas in Kelvin. The diffusion that a free electron undergoes in a gas is due to random collisions with the gas molecules. If the gas is not influenced by an electric field, then the diffusion is isotropic and follows a Gaussian distribution. An initial point-like electron cloud at $r \sim 0$ will follow, and at time t, the density distribution will be:

$$\phi(\mathbf{r}, t) = \frac{1}{(\sqrt{2\pi}\sigma)^3} e^{-\frac{(\mathbf{r}-r_0)^2}{2\sigma^2}} \tag{2.16}$$

where the sigma of the distributions is defined as:

$$\sigma^2 = 2\bar{D}t \tag{2.17}$$

with $\bar{D}$ being the mass diffusivity.

When a constant electric field is applied to the gas, the electron cloud undergoes a constant drift motion in addition to the thermal diffusion. When there is no magnetic field, as is the usual case in RPCs, the direction of motion follows the electric field lines. As the presence of an electric field implies the addition of a constant drift motion to the thermal diffusion, the diffusion becomes anisotropic. We can assume a rotational symmetry around the electric field axis for the electron cloud, and using cylindrical coordinates we obtain from **equation 2.16**:

$$\phi(r, z, t) = \frac{1}{\sqrt{2\pi}\sigma_L\sigma_T^2} exp\Big(- \frac{(z-z_0)^2}{2\sigma_L^2} - \frac{(r-r_0)^2}{2\sigma_T^2} \Big) \tag{2.18}$$

We can separate **equation 2.18** in two distinct terms, a longitudinal term and a transverse term:

$$\phi(z, t) = \frac{1}{\sqrt{2\pi l}D_L} e^{-\frac{(z-z_0)^2}{2D_L^2 l}} \tag{2.19}$$

$$\phi(r, t) = \frac{1}{D_T^2 l} e^{-\frac{(r-r_0)^2}{2D_T^2 l}} \tag{2.20}$$

Both equations define the density distribution of an electron cloud in the longitudinal and transverse plane (parallel and perpendicular to the electric field lines, respectively) due to the diffusion of electrons with the gas molecules **[6]**.

2.2.7 Electrical Field Strength

In the simplified case of a uniform parallel plate gap with a constant applied voltage, the voltage between the electrodes is:

$$\Delta V = E_r \cdot d = \frac{E_0}{\varepsilon_r} d \tag{2.21}$$

where E_r is the electrical field in a dielectric medium with a permitivity ε_r, E_0 is the electrical field inside the gas gap and d the gap separation.

These can be extended to several dielectrics. Assume a configuration with k gaps and $k+1$ electrodes. This can be thought of as various parallel plate capacitors in series consisting of $2k+1$ layers:

$$\Delta V = \sum_{i=1}^{2k+1} E_i d_i \tag{2.22}$$

Supposing that the gas gap width is g with a relative permitivity $\varepsilon_g \sim 1$ and electrical field strength E_g, the electrodes' width b with relative permitivity ε_b and electrical field strength E_b results in:

$$\Delta V = (k+1) b E_b + k g E_g \tag{2.23}$$

Using the boundary condition at the interface of the gas gap and the electrode for the normal components of the electrical field we obtain:

$$E_b \varepsilon_b = E_g \varepsilon_g \tag{2.24}$$

$$\rightarrow E_g = \frac{\Delta V}{\frac{(k+1)}{\varepsilon_b} b + k g} \tag{2.25}$$

This configuration results in a uniform electrical field through the gas gap and with a constant value for every single one of the k gaps. The same can also be concluded for the electrical field in the electrodes [**5**].

2.2.8 Ramo's Theorem

Ramo's theorem states that the current i_{ind} on an electrode induced by a moving point charge q is given by:

$$i_{ind}(t) = q\boldsymbol{\nu_d} \cdot \boldsymbol{E_w}(\boldsymbol{x(t)}) \tag{2.26}$$

To demonstrate this theorem, let us begin by considering the configuration in **Fig. 2.3**. This setup includes a series of k electrodes, each at its respective voltage, with a charge Q moving freely between them and space charge ρ, denoted by the darker color in the background.

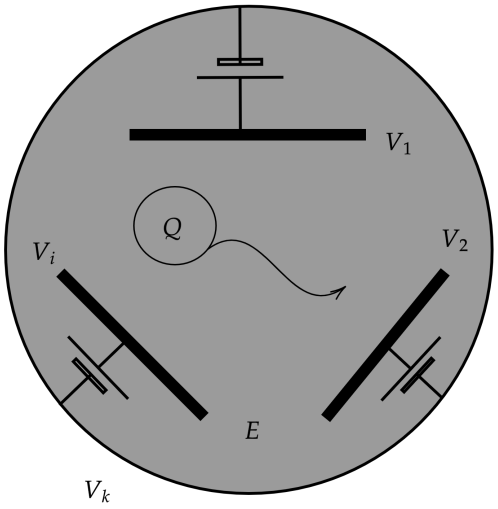

Figure 2.3: Setup for the proof of Ramo's Theorem.

Due to the superposition principle, we can divide the configuration in two: one keeping the actual potentials but removing the charges, with the other grounding the electrodes but keeping the charges, as shown in **Fig. 2.4**:

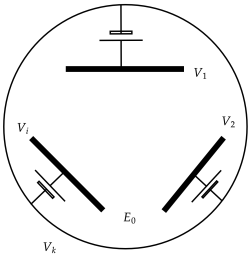

(a) Configuration without charges, but with potentials.

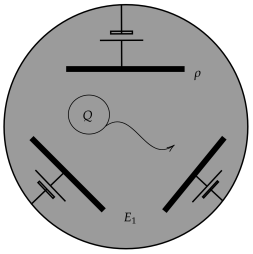

(b) Configuration with charges and grounded electrodes.

Figure 2.4: Superposition principle applied to the setup

Starting with the configuration (b), where all the electrodes are grounded, the work done by the electric field as the charge moves from a position x_i to x_f is:

$$W = \int_{x_i}^{x_f} Q\boldsymbol{E_1'} \cdot d\boldsymbol{x} \tag{2.27}$$

where $\boldsymbol{E_1'}$ differs from $\boldsymbol{E_1}$ in the exclusion of the field generated by Q only. As the charge moves, the induced charge in the electrodes redistributes accordingly to a zero potential, since they are grounded. This implies that there is no energy exchange between the power supply and the system. Using conservation of energy and the energy density we also obtain:

$$w = \frac{1}{2}\varepsilon E^2 \tag{2.28}$$

$$\rightarrow W = \frac{1}{2}\int_\tau \varepsilon(E_{1f}^2 - E_{1i}^2)d\tau \tag{2.29}$$

where $\boldsymbol{E_{1f}}$ and $\boldsymbol{E_{1i}}$ are the electrical fields at the final and starting positions,ε the relative permittivity and the integral is done over the volume of the setup. If we apply this to the current configuration where $\boldsymbol{E = E_0 + E_1}$:

$$W_{field} = \int_{x_i}^{x_f} Q(\boldsymbol{E_0} + \boldsymbol{E_1'}) \cdot d\boldsymbol{x} \tag{2.30}$$

However, unlike configuration (b), the total work done by the power supplies is given by:

$$W_{supplies} = \sum_{i=1}^{k} V_i Q_i \tag{2.31}$$

where V_i and Q_i are the ith electrode voltage and induced charge respectively.

The increase in the electric field energy due to energy conservation is expressed as follows:

$$\Delta W = W_{supplies} - W_{field} = \sum_{i=1}^{k} V_i Q_i - \int_{x_i}^{x_f} Q(\boldsymbol{E_0} + \boldsymbol{E_1'}) \cdot d\boldsymbol{x} \tag{2.32}$$

$$= \frac{1}{2}\int_\tau \varepsilon[(\boldsymbol{E_0} + \boldsymbol{E_{1f}})^2 - (\boldsymbol{E_0} + \boldsymbol{E_{1i}})^2]d\tau$$

Utilizing Green's first identity:

$$\int_s \Phi(\nabla\Psi) \cdot d\boldsymbol{a} = \int_\tau [\Phi\nabla^2\Psi + (\nabla\Phi) \cdot (\nabla\Psi)]d\tau \tag{2.33}$$

$$\rightarrow \int_\tau \boldsymbol{E_0} \cdot \boldsymbol{E_1} d\tau = \int_\tau (\nabla\phi_0 \cdot \nabla\phi_1)d\tau \tag{2.34}$$

$$= \int_s \phi_1(\nabla\phi_0) \cdot d\boldsymbol{a} - \int_\tau \phi_1\nabla^2\phi_0 d\tau$$

Assuming that the electrical field for each configuration should be the gradient of a potential ϕ, we arrived to the following equation:

$$\boldsymbol{E} = -\nabla\phi \tag{2.35}$$

Since all electrodes are grounded in configuration (b), ϕ_1 is zero along the surface. Likewise, in configuration (a) there is no charge so the charge density is zero ($\nabla^2\phi_0 = 0$). These lead us to conclude that **equation 2.34** is zero.

Thus the increase in the field energy is:

$$\Delta W = \frac{1}{2}\int_{\tau} \varepsilon(E_{1f}^2 - E_{1i}^2)d\tau \tag{2.36}$$

which is the same as in the configuration without the charges. Substituting these expressions into **equation 2.32** we find that:

$$\sum_{i=1}^{k} V_i Q_i = \int_{x_i}^{x_f} Q\boldsymbol{E_0}\cdot d\boldsymbol{x} = -Q[\phi_0(x_f) - \phi_0(x_i)] \tag{2.37}$$

If we wanted to know specifically the induced charge in a single electrode M, we can set all of the other voltages to zero and the voltage of the electrode M to one. The induced charge then reduces to:

$$Q_M = -Q[\phi_0(x_f) - \phi_0(x_i)] \tag{2.38}$$

Meaning that the induced current is:

$$\rightarrow i_M = \frac{dQ_M}{dt} = Q\,\boldsymbol{E_0(x_f)}\cdot\frac{d\mathbf{x}}{dt} = Q\boldsymbol{\nu}\cdot\boldsymbol{E_0(x_f)} \tag{2.39}$$

Relabeling the expression:

$$i_{ind}(t) = q\boldsymbol{\nu_d}\cdot\boldsymbol{E_w(x(t))}$$

as desired so Ramo's Theorem is proved. This proof and some applications of Ramo's Theorem can be found in [**7**].

The term $\boldsymbol{E_w}$ is called the "weighting field", where we put all electrodes to zero except the one of interest. As such, it has dimensions of inverse length. Knowing this, we can use **equation 2.25** to obtain the magnitude of the weighting field of a Multi-gap Resistive Plate Chamber with k gaps, gap width g, electrode width b and relative permitivity ε_b:

$$E_w = \frac{1}{\frac{(k+1)}{\varepsilon_b}b + kg} \tag{2.40}$$

With the use of Ramo's Theorem we can calculate the induced current of an avalanche of electrons crossing the gap perpendicularly:

$$I_e(t) = q_e N_e(t)\frac{\nu_e}{\frac{(k+1)}{\varepsilon_b}b + kg} \tag{2.41}$$

where $N_e(t)$ is given by:

$$N_e(t) = N_0 e^{\alpha^*\nu_e t}\Theta(\frac{g - x_0}{\nu_e} - t) \tag{2.42}$$

In this expression x_0 is the position where the primary cluster was created, N_0 the number of primary clusters produced and Θ is the *Heaviside Step function.* α^*, the effective Townsend coefficient, is defined as:

$$\alpha^* = \alpha - \eta \tag{2.43}$$

where η is the attachment coefficient, which decreases for higher electrical field strength.

If we integrate this expression we can obtain the induced charge caused by the electron drift:

$$Q_e^{ind} = \int_0^{x_0/\nu_e} I_e(t)dt = \frac{q_e\nu_e}{\frac{(k+1)}{\varepsilon_b}b + kg} \times \frac{N_0 e^{\alpha^*\nu_e t}}{\alpha^*\nu_e} \Bigg|_0^{x_0/\nu_e}$$

$$= \frac{q_e N_0}{\alpha^*} \frac{e^{\alpha^* x_0} - 1}{\frac{(k+1)}{\varepsilon_b}b + kg} \tag{2.44}$$

Meanwhile for the positive ions their ion density is:

$$n_{I+}(x,t) = N_0\alpha e^{\alpha^*(x+\nu_i t)}[\Theta(x-\nu_i t) - \Theta(x-x_0-\nu_i t)]$$

Integrating over the distance and applying Ramo's Theorem, we obtain:

$$I_{ions}(t) = \frac{q_e\nu_i}{\frac{(k+1)}{\varepsilon_b}b + kg}\left[1+\frac{\alpha}{\alpha^*}\Big(e^{\alpha^* x_0}-1\Big)-\Big(1+\frac{\alpha}{\alpha^*}\Big(e^{\alpha^*(x_0-g+\nu_i t)}-1\Big)\Big)\Theta(x_0-g+\nu_i t)\right]\Theta(g-\nu_i t) \tag{2.45}$$

By integrating over time we can similarly calculate the induced charge:

$$Q_{ions}^{ind} = \frac{q_e N_0}{\frac{(k+1)}{\varepsilon_b}b + kg}\left[\frac{\alpha}{\alpha*}\Big((\alpha^* g - 1)\frac{e^{\alpha^* x_0} - 1}{\alpha^*} + x_0\Big) + g - x_0\right] \tag{2.46}$$

For the simple case of a single gap and the simplification of $x_0 = g = d$ this reduces to:

$$Q_e^{ind} = N_0 q_e \frac{e^{\alpha^* d} - 1}{\alpha^* d} \tag{2.47}$$

$$Q_{ion}^{ind} = N_0 q_e \frac{e^{\alpha^* d}(\alpha^* - 1) + 1}{\alpha^* d} \tag{2.48}$$

where the total signal is given by:

$$Q_{ion}^{ind} + Q_e^{ind} = N_0 q_e e^{\alpha^* d} \tag{2.49}$$

and the fast to total ratio tends to:

$$\frac{Q_e^{ind}}{Q_{ion}^{ind} + Q_e^{ind}} \approx \frac{1}{\alpha^* d} \tag{2.50}$$

This relation holds under the condition of high gas gain, i.e. $e^{\alpha^* d} >> 1$.

Unfortunately this approach does not take into account electron diffusion, homogeneous ionization across the gap or space charge affecting avalanche growth. A modified version of these expressions can be found in [**4**], in which:

$$q_{ind} = \frac{q_e}{\eta g} V_w n_0^j M_j \Big[e^{\eta(x_{sat} - x_0^j)} - 1\Big] + M_j V_w \frac{g - x_{sat}^j}{g} q_{sat} \tag{2.51}$$

In this expression V_w is the drop of the weighting voltage across the gap, n_0^j is the number of clusters involved, M_j is a factor that takes into account the avalanche growth fluctuations, q_{sat} is the value of charge at which the avalanche stops its growth and simply drifts to the anode and x_{sat}, the position at which this charge saturation occurs, is given by:

$$x_{sat}^j = x_0^j + \frac{1}{\alpha^*} log\Big(\frac{q_{sat}}{q_e n_0^j}\Big) \tag{2.52}$$

2.2.9 Space Charge

When a charged particle enters the gap, it creates a path of ionization that can trigger an avalanche process. The avalanche consists of two parts, a head of fast moving electrons and a tail of slow positive ions. As the amount of particles grows large enough, their presence can alter the electrical field in their surroundings affecting their drift velocity and the effective Townsend coefficient, consequently distorting the uniform field across the gap. This large presence of charge is called the **space charge**.

The presence of space charge impacts on the signal retrieved and thus the amount of charge measured, mainly because these charge clusters change drastically the local electrical field surrounding them as illustrated in **Figure 2.5**. This is particularly true for the Multigap Resistive Plate design where the reduced gap allows for a stronger electrical field strength but also a higher space charge density due to the avalanche occurring over a smaller distance and thus higher space charge.

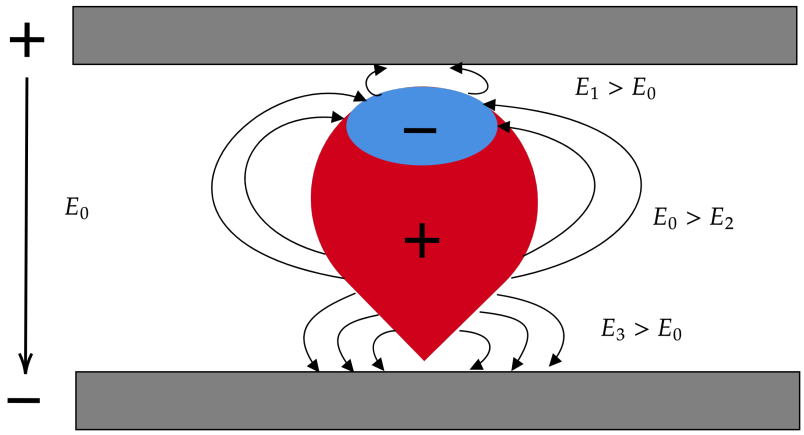

Figure 2.5: Schematic of an avalanche and its effect on the electrical field strength. The electric field is reduced between the electron cloud head and the positive ions and increased in front the anode.

The space charge has two main consequences: the change of the local gas gain around it and the increased appearance of large pulses called "streamers". The streamer formation produces a number of observable effects such as:

- Linearization of the induced charge growth and deviation of the exponential behaviour.
- The increment on the fast to total charge ratio compared to the approximation in **equation 2.11**.

More information about the space charge effects and their implications can be found in [**8**] and [**9**].

Various approaches to treat the space charge can be attempted, but the general behaviour is that for small voltages the progression is exponential as in a Townsend avalanche, but as the amount of charge increases the space-charge effect linearizes the curve.

One of these approaches, and the most common, consists in the linearization of two segments of the avalanche charge by implementing a certain threshold voltage ΔV_0. The first part up to the voltage threshold is a zero region or almost negligible for practical terms, while after that approaches the space charge regime with certain slope k_s.

$$n_e = \begin{cases} 0 & \Delta V_{gap} \leq \Delta V_0 \\ k_s(\Delta V_{gap} - \Delta V_0) & \Delta V_0 < \Delta V_{gap} \end{cases}$$

The idea of this model is shown in **Figure 2.6**.

Another approach involves modifying the effective Townsend coefficient α^*. This consist in a decrease of the effective Townsend coefficient as a function of the avalanche charge depending on a saturation charge threshold, where n_{sat} is the number of electrons involved in this threshold:

$$\alpha^*_{per} = \begin{cases} \alpha^* & n_e \leq n_{sat} \\ \alpha^*(1 - B_s ln(\frac{n_e}{n_{sat}})) & n_{sat} < n_e \end{cases}$$

B_s is a dimensionless shape parameter related to the sharpness of the transition. These models and some solutions of the second approach can be found in [4].

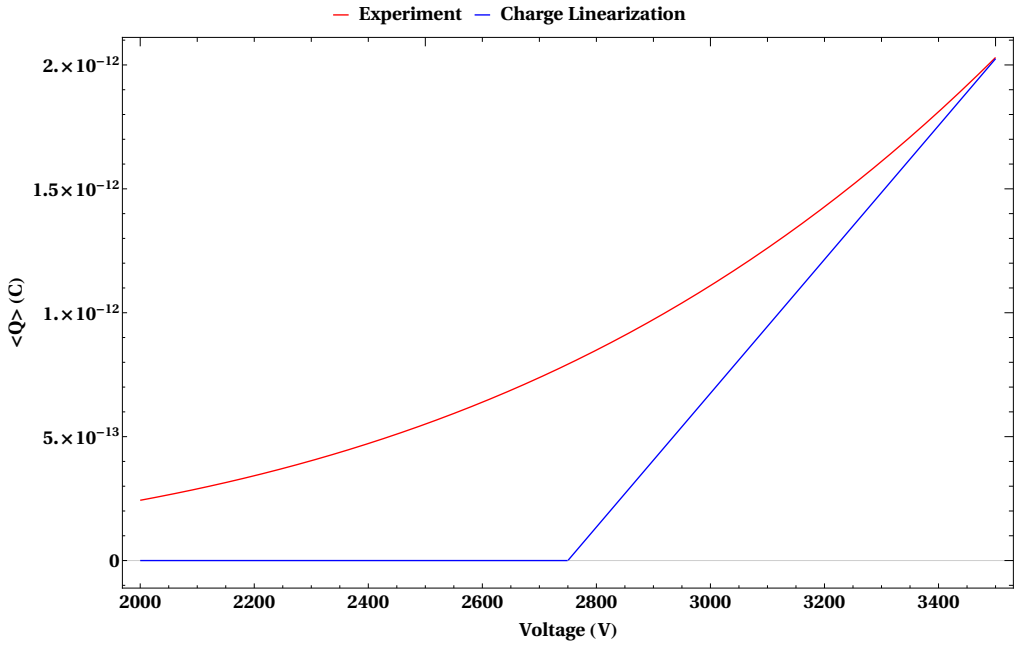

Figure 2.6: Scheme showing the charge linearization model of the first approach and the average charge from a single 3mm gap.

2.3 Streamer and Avalanche Mode

As reviewed above, as the avalanche reaches a certain threshold (the so-called Raether limit, around a gas gain of 10^8) it evolves into a **streamer**. When this occurs a column of charges between the anode and cathode has formed, stopped by the resistive plates preventing the discharge.

An RPC operating in **streamer mode** allows an avalanche to evolve into a streamer, normally without letting it grow large enough to produce a discharge. The streamer mode requires higher electrical fields to be applied inside the gap, causing the effective Townsend coefficient to increase and reach the desired limit. In order to increase the electrical field inside the gap and consequently achieve a higher effective Townsend coefficient, various methods can be used. The most obvious of these is to increase the voltage applied to the gap, although this can also be achieved by reducing the gap sizes without changing the operating voltage.

The signal produced in this mode consequently is much larger than a simple avalanche and can be retrieved without the need of an amplifier. However, due to the higher amount of charges produced, a higher current flows through the resisitive plates causing a voltage drop and thus the chamber requires a longer relaxation time. This time is needed in order for the region of the avalanche to be sensitive again, resulting in an inability to work at higher rates.

With the necessity of achieving higher efficiencies utilizing higher rates, the **avalanche mode** was implemented. The avalanche mode operates at lower voltages, thus not reaching the Raether limit and reducing the probability of a transition to a streamer. A smaller amount of charge accumulated in each gap gives a better efficiency, whose immediate benefit is to increase the rate capability. The main disadvantage with this is a reduced signal due to the reduction in charge, so an amplifier is needed to retrieve the signals, requiring more complex electronics.

This can be achieved by reducing the applied voltage but a more interesting approach is the use of electronegative gases such as freon, which can absorb some of the electrons created in the avalanche, producing slow negative ions or quenching gases like SF_6, where even small amounts can make a difference in the total amount of charge.

Chapter 3

Experimental Setup

3.1 MRPC Construction

Two Multi Gap Glass Resistive Plate Chambers were used with different gas gap widths, 120 μm and 160 μm, 20 gaps with a double stack configuration. Each stack has 2 outer glass sheets of dimension 22x22 cm^2 and 9 inner glasses of dimension 18x18 cm^2, and a thickness of 0.28 mm. An area of 18x18 cm^2 in the outer glass sheets had been painted with resistive coating with a surface resistivity of $5M\Omega/\square$. All glass sheets had a bulk reistivity of $1.3 \times 10^{12}\Omega cm$ at $24°C$. The spacers used for the glass are mono filament commercial nylon fishing lines. A Mylar sheet was placed between the voltage electrodes and the printed circuit boards (PCBs) to isolate the high voltage. Three PCBs with pick-up strips are used to readout the signals from the MRPC. The two resistive electrodes next to the PCB were connected with negative high voltage and the other two electrodes on the top and bottom layer connected to positive high voltage. The MRPC therefore has two anode pickup strip planes (top and bottom) and one cathode pick-up strip plane (middle). The two anode strip planes are connected, adding the signals of the two stacks together. The width of the pick-up strip is 1 cm on a pitch of 1.1 cm. The length of the strip is 21 cm. Two honeycomb panels are attached to the top and bottom layer of MRPC for mechanical support. The two MRPCs are mounted inside a gas-tight aluminium box [**10**].

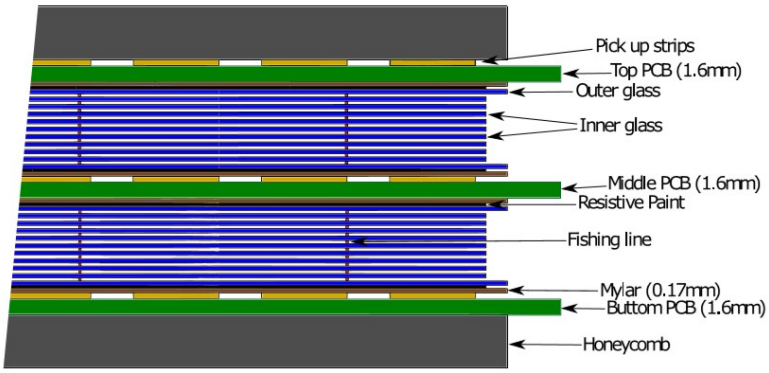

Figure 3.1: Cross section of the double stack 20-gap MRPC [**10**].

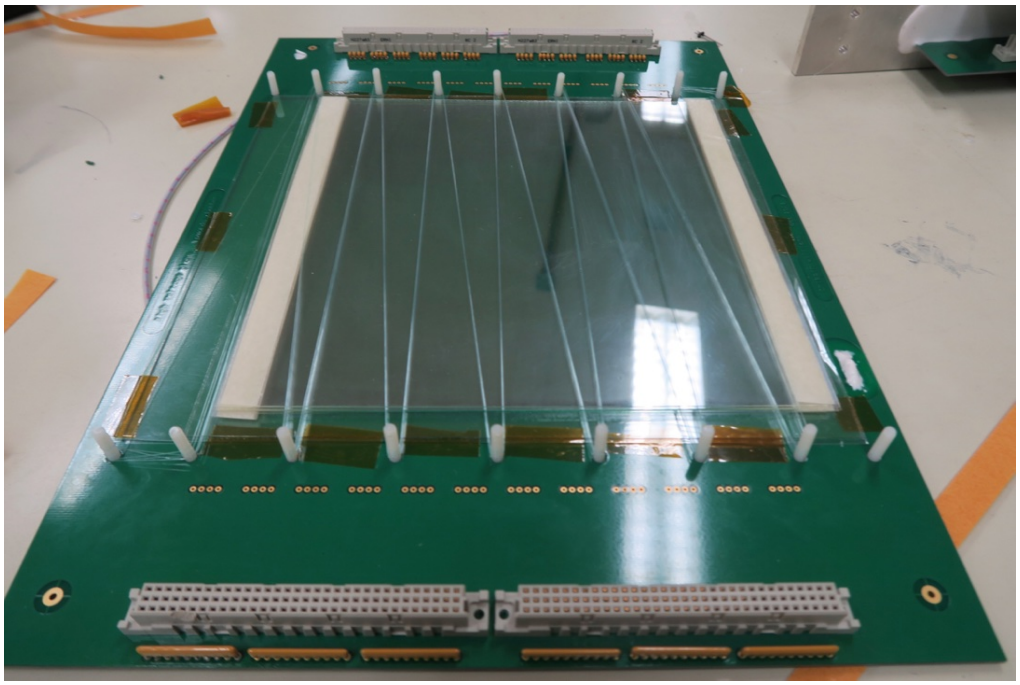

Figure 3.2: One open Multigap Resitive Plate Chamber. Although this is not the one tested, the overall construction is nearly identical.

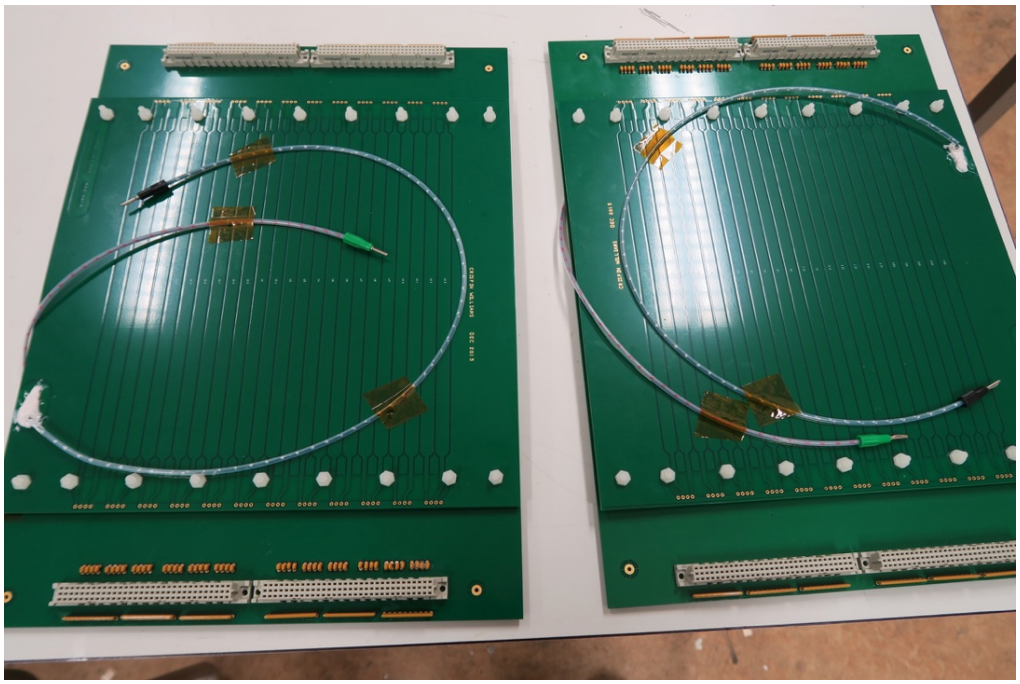

Figure 3.3: Two finished Multigap Resitive Plate Chambers that are ready to be put inside the aluminum box.

3.2 Setup

The chambers were placed in a scintillator telescope, consisting of three scintillators of various dimensions. The top scintillators encompassed an overlapping area of 8x8 cm^2, covering approximately 4 broad strips that were used to establish when cosmic rays pass through. The chambers were placed between the two scintillators as well as the one on the bottom. The scintillators were connected to a high voltage power supply providing 1.75 kV to each. An scheme of this setup is shown in **Figure 3.4**.

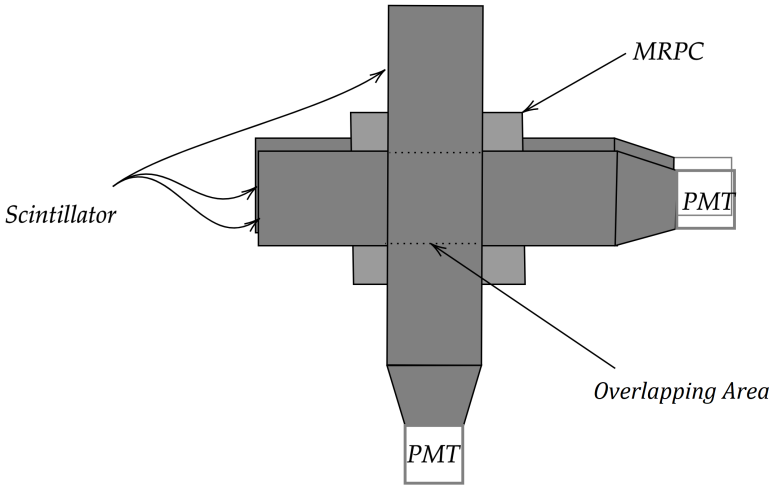

Figure 3.4: Upper view of the MRPC and telescope arrangement.

Gas pipes were connected to a mass flow controller providing a mixture of 95% Freon and 5% SF_6 at 60% of the maximum flow of the controller. This was connected directly to the chamber under test and then in series to the rest of the chambers. The chamber was also connected to a DC high voltage power supply providing voltage in a range of 9 up to 10 kV individually to the anode and cathode, effectively doubling the total effective voltage. This can be seen in the scheme in **Figure 3.5**

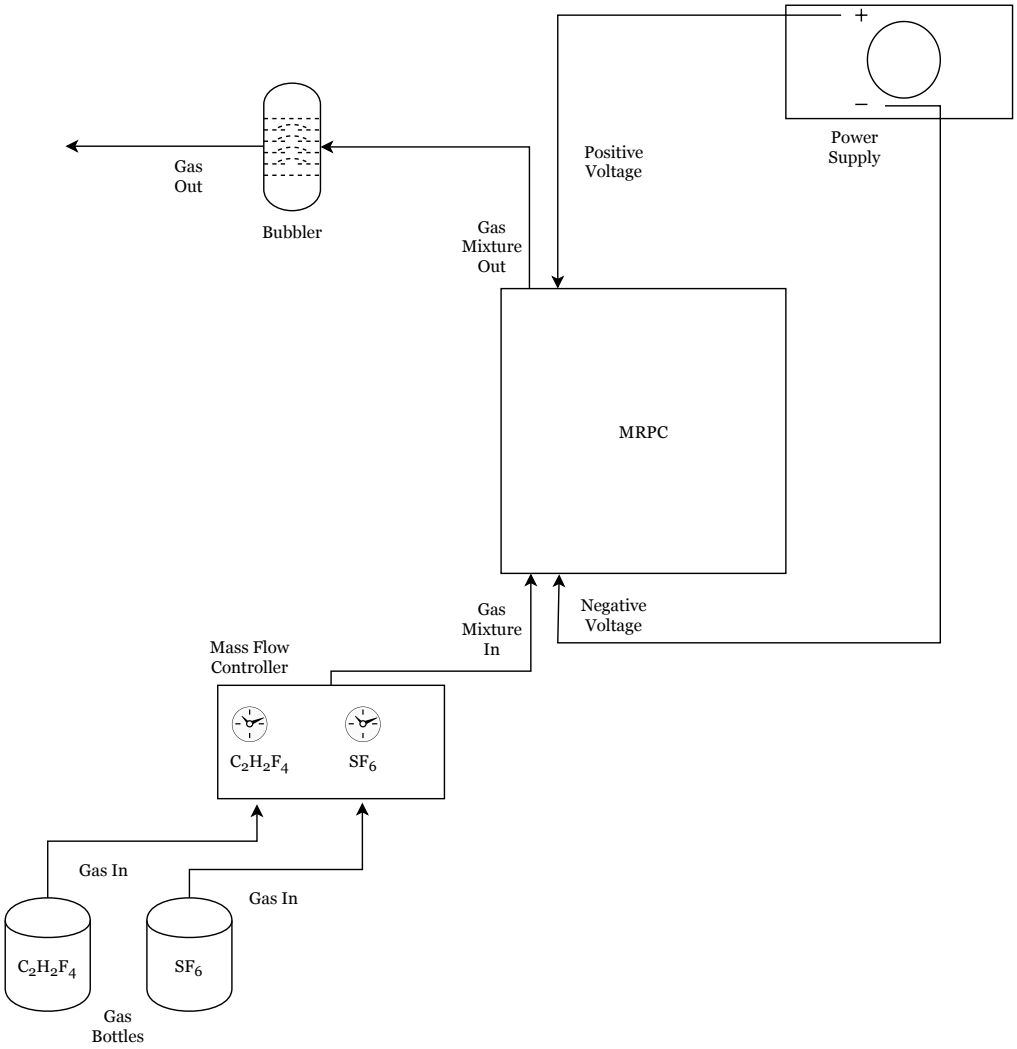

Figure 3.5: Scheme of the experimental setup including the gas lines.

Each scintillator was connected to a LeCroy standard discriminator unit via LEMO cables to rate the signal. The discriminator was also connected to a LeCroy standard coincidence unit, so that the signals of the three coincided. The coincidence unit was then connected to a LeCroy timer unit which finally was connected to an oscilloscope with a 50 Ω resistance coupling. Meanwhile, the chamber was connected to the oscilloscope through PCB adapters via 8 pin connectors and adapted to a LEMO 00 cable that was plugged in to the oscilloscope coupled with a 1 $M\Omega$ resistance to avoid charging the pickup strips. This setup is shown in **Figure 3.6**.

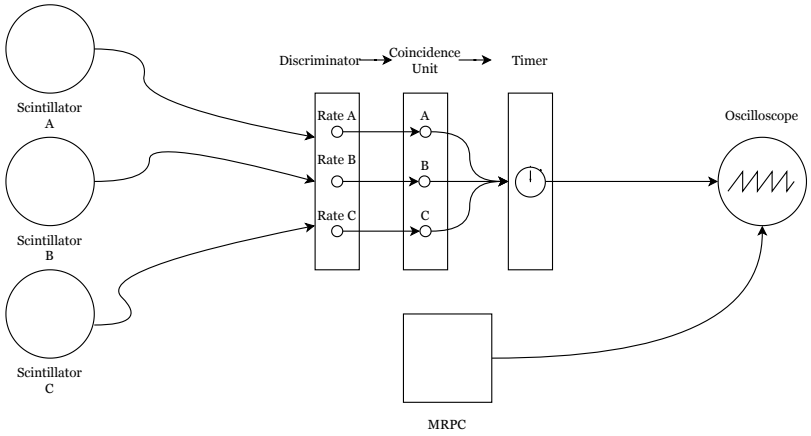

Figure 3.6: Scintillators logical setup. The scintillator signal is taken to a discriminator unit, coupled with a coincidence unit that through at timer send the trigger signal to the oscilloscope.

The experimental setup including: HV cables in red, gas pipes in white, PMTs and scintillators in black, MRPC in grey and oscilloscope cables in yellow, is shown in **Figure 3.7**:

Figure 3.7: Experimental setup.

The cables that are connected to the electrodes are short and share the same length to minimize the effect of reflections. They are further grounded to minimize noise. For similar reasons the length of the PMT (Photo Multiplier Tube) cables was also the same, which allows one to avoid the use of delays in order to obtain coincidences.

Chapter 4

Experimental Results

4.1 Measurement of the Signal

As the particles that ionize the gas pass through, the avalanche induces a charge in the electrodes and produces a signal. This process happens multiple times, at a certain rate, so it is of importance to know the total amount in order to understand the phenomena that take place inside the chamber and their evolution. One of the most important phenomenon, the avalanche growth, is somewhat limited by the effects of the space charge, enhancing the rate capability of the detector. By studying the increase of the fast charge over the total charge we can have an idea of how these compare in the case of the streamer formation.

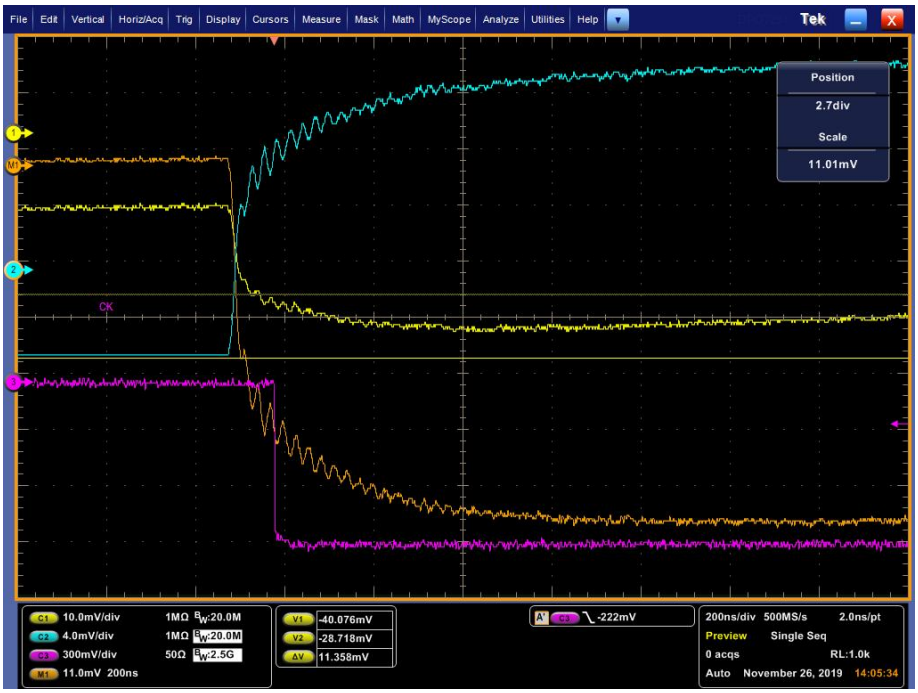

Figure 4.1: Signal retrieved in the oscilloscope. The yellow graph shows the signal in the anode, the blue in the cathode, the orange shows the differential signal and the purple denotes the trigger.

The chambers were connected to a high voltage power supply applying voltages from 9 to 11 kV and placed between a scintillator telescope. In this way, whenever a particle generates a coincidence, the signal in mV is retrieved by the oscilloscope.

These measurements were repeated 200 times for each voltage and for the two chambers. The height of the fast signal and the slow signal was retrieved from which the ratio could be calculated. Once the data for a voltage was retrieved, the voltage from the power supply was changed, after which approximately half an hour of waiting was needed to allow for stabilization of the gas flow.

From **Fig. 4.1** we can clearly distinguish the two parts that form the signal:

- The fast signal is associated with the steep slope that is due to the fast drift velocity of the electrons towards the anode.
- The slow signal is associated with the slow ramp after the linear slope due the slow drift of the positive ions towards the cathode.

From the figure we can also obtain the fast to total ratio. In this case the fast signal height is about 5 squares (where the scale in this case is 11 mV per square) with the total being around 6 squares, so that their ratio is around 83%, indicating that this corresponds to a streamer. Additionally, we can see that the signal starts at the same time for both the cathode and anode, meaning there is no delay of the signal between them (in reality the interaction happens at the speed of light, making the delay negligible in this case).

4.2 Measurement of the Capacitance

The capacitance of the detector is the ratio between the charge accumulated in the capacitor and the difference in the potential field across the plates:

$$C = \frac{Q}{V} \tag{4.1}$$

where C is the capacitance, Q is the charge in the plates and V is the electrical potential.

In order to calculate the charge Q, the capacitance of the detectors is required. To obtain this quantity -the same experimental setup was used- with the help of a multimeter without applied voltage from the power supply.
The basic idea is to think of the setup as an RC circuit, satisfying:

$$C\frac{dV}{dt} + \frac{V}{R} = 0 \tag{4.2}$$

which has the solution:

$$V = V_0 e^{\frac{-t}{RC}} \tag{4.3}$$

where R is the resistance and V_0 is the voltage at time $t = 0$.

With this in mind, we first measured the resistance R between the electrodes with the multimeter using the 8 pin connectors. We then applied a constant current to them with the voltmeter taking advantage of the principle that the multimeter uses to measure the voltage. In this way the voltage rises linearly, as:

$$C = \frac{Q}{V}$$

$$\rightarrow I \equiv \frac{dQ}{dt} = C\frac{dV}{dt} \tag{4.4}$$

$$\rightarrow \int Idt = C\int dV \tag{4.5}$$

$$\rightarrow CV = It + const \tag{4.6}$$

After certain amount of time, the voltage should reach a constant value. This behaviour was observed with the oscilloscope .

After we cut the applied current, the discharge of the electrodes commences, decaying exponentially as predicted by **equation 4.3**. This can be seen in **Figure 4.2**.
By retrieving data from the discharge, fitting an exponential to it and obtaining the value of the exponent, we obtained the capacitance as:

$$\frac{1}{RC} \approx 10792 s^{-1} \tag{4.7}$$

$$\rightarrow \frac{1}{C} \approx 5 \times 10^5 \Omega \times 10792 s^{-1} \tag{4.8}$$

$$\rightarrow C \approx \frac{1}{5 \times 10^5 \Omega \times 10792 s^{-1}} \approx 185 pF \tag{4.9}$$

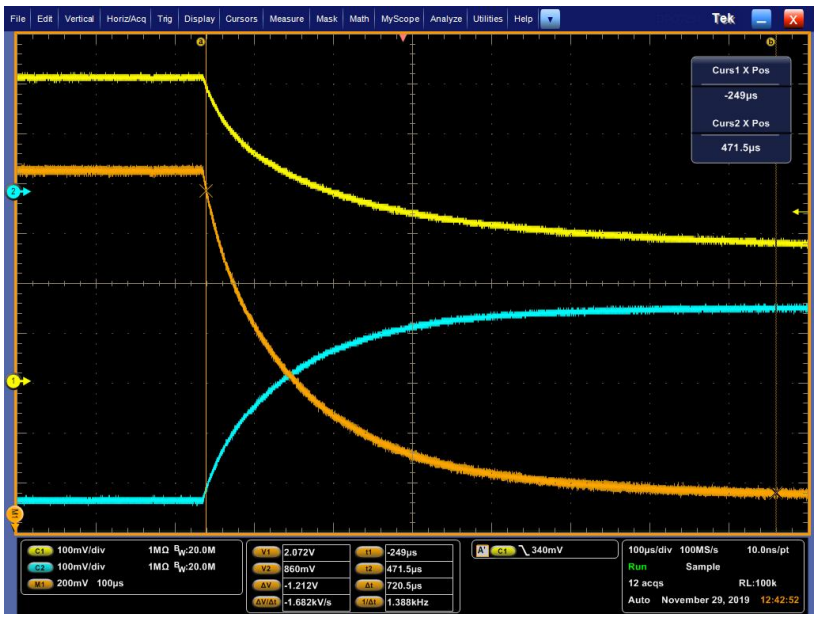

Figure 4.2: Voltage measurement of electrode discharge obtained with the oscilloscope. The yellow graph shows the voltage at the anode, the blue graph at the cathode and the orange graph shows the sum of both.

The same process was repeated on the other chambers to finally obtain a value of a capacitance around 185 pF and 166 pF for the 120 μm gap and 160 μm gap chambers respectively.

Gap Size (μm)	**Capacitance** (pF)
120	185
160	166

Table 4.1: Capacitance of the two different MRPC gap sizes.

4.3 Analysis Procedure

As previously stated the fast signal corresponds to the steep slope which includes the quick drift of the electrons. The total signal includes both the electrons as well as the positive ions. We finally also consider their ratio, which is the fast charge divided by the total charge.

The charge can be obtained using the relationship between the voltage and the capacitance:

$$Q = CV \tag{4.10}$$

The mean fast and total charges for each voltage were calculated by:

$$\bar{Q} = \sum_{i=0}^{N} \frac{q_i}{N} \tag{4.11}$$

and the deviation from the mean as:

$$\sigma = \frac{\sigma_x}{\sqrt{N}} \tag{4.12}$$

where $\bar{Q}$ is the average charge for the fast or total depending on the case, q_i is the charge of the ith event, N is the number of measurements. The standard deviation, σ_x, is given by:

$$\sigma_x = \sqrt{\frac{\sum_{i=0}^{N}(\bar{Q} - q_i)^2}{N-1}} \tag{4.13}$$

For the fast to total ratio, each individual signal was used to obtain it's ratio and the average for each voltage calculated as:

$$R = \frac{1}{N} \sum_{i=0}^{N} \frac{q_i}{Q_i} \tag{4.14}$$

where for this case q_i and Q_i denotes the fast charge and total charge of the ith signal respectively.

4.4 Charge Distribution

The avalanche size arises from a stochastic process, as does the amount of charge. However, this amount is not equally distributed. As we retrieve events, a certain distribution of the amount of the charge can be obtained. **Figure 4.3** and **Figure 4.4** depict histograms of both the fast and total induced charge for both of the 120 and 160 μm gap configurations. A very noticeable pattern emerges, in which a Gamma distribution used as an extension to the Poisson distribution fits the histograms. This is perhaps directly related to the cosmic ray distribution that presents a similar distribution.

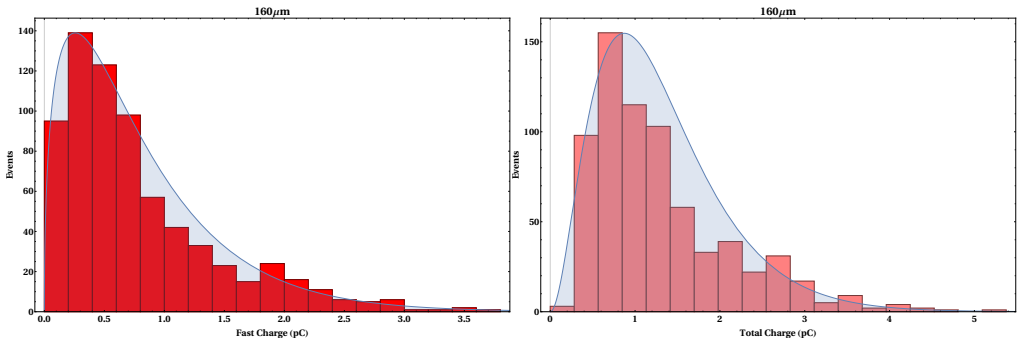

(a) Fast charge distribution **(b)** Total charge distribution

Figure 4.3: Charge distribution of the 160 μm configuration.

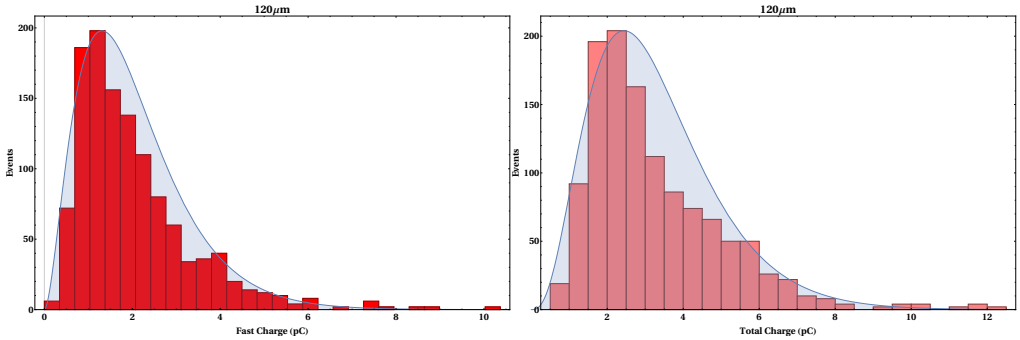

(a) Fast charge distribution **(b)** Total charge distribution

Figure 4.4: Charge distribution of the 120 μm configuration.

The distribution seems to behave similarly for both chambers. However, the charge range is wider for the narrower gap for both fast and total charge distributions. This behaviour is expected to appear in the averages in later sections. The average total charge for the narrower gap is around the 3.3 pC, while the wider gap is 1.3 pC, a reduction of almost 60 percent. Meanwhile, the average fast charge is 2.04 and 0.785 pC for the 120 and 160 μm gaps respectively, presenting a reduction, again, of 60 percent. Nevertheless, it is apparent that more data is needed to improve the distribution.

4.5 Fast Charge to Total Ratio

In this section we study the fast induced charge produced by the drifting electrons inside the gap. We compare it with the total charge, induced by the drifting ions, to obtain their ratio. Finally we study the behaviour of this ratio as a function of the fast charge.

For a single gap RPC that operates in the avalanche mode, the fast charge to total charge ratio expected would be around 5%. Normally due to this, the fast charge for the electrons can be neglected, however this ratio increases significantly for the case of an MRPC.

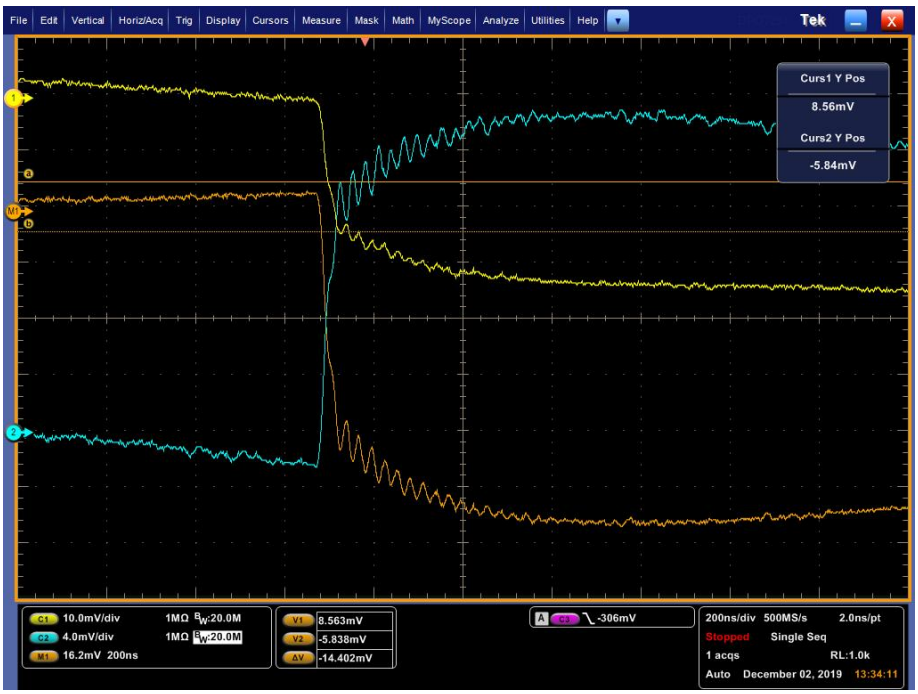

Figure 4.5: Streamer signal retrieved by the oscilloscope.

From **Fig. 4.5** we notice that after the linear ramp a slow ramping curve follows. It is reasonable that the slow ramp from the positive ions does not correspond to a linear behaviour, since for this to occur the ions would have had to form at the same point. Instead, we can assume that the positive ions are created over a region and not just a point. This is the case for the electrons as well, as they are created in pairs but, unlike the positive ions, their fast movement produces more linear behaviour in the signal.

The ratios of these signals were retrieved and used to obtain the behaviour of the average ratio with respect to the fast charge. The result of the average ratio is independent of the units of the signal, due to the relation between the voltage and the charge.

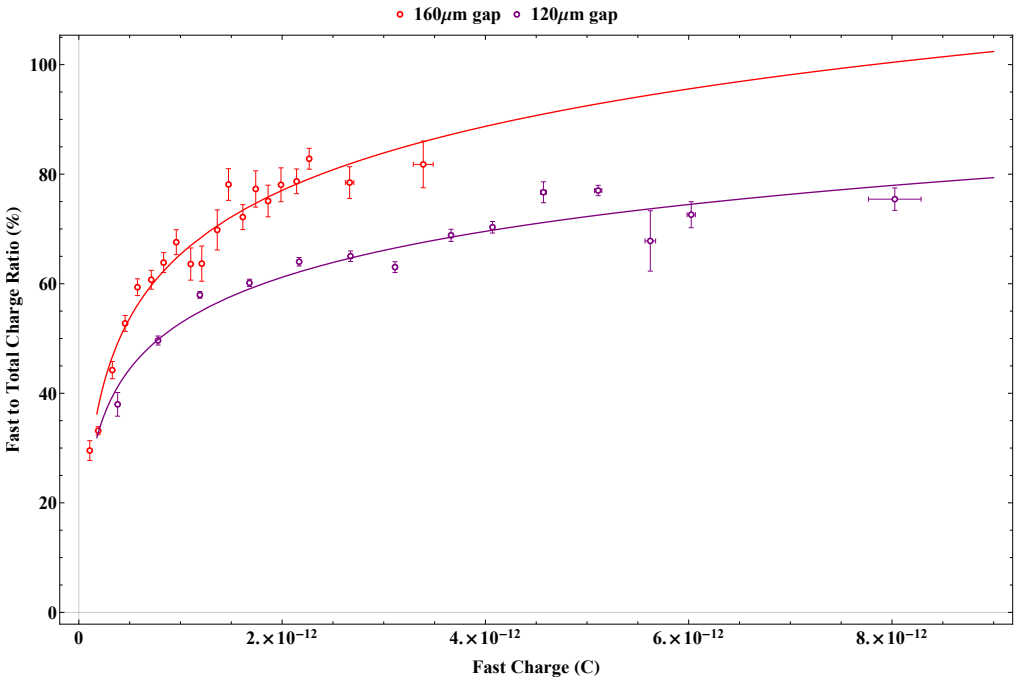

Figure 4.6: Average fast to total charge ratio as a function of the fast charge for the 120 μm and 160 μm chambers. The lines are just a rough estimate to guide the eye.

Fig. 4.6 shows that as the fast charge increases, the fast to total charge ratio also increases and the behaviour of both chambers seems to be the same. This means that there is no significant difference in the mechanism of the avalanche formation for the two chambers.

The ratio between the gap widths of the two chambers is 25%. Thus there is an increase of the 25% in the strength of the electric field for the chamber with narrower gap for the same applied voltage. A higher electrical field increases the gas gain, which produces an increase in the number of electrons during the formation of the avalanche. This could be one of the reasons for the higher average fast charge in the narrower gap, reaching values as much as doubled compared to the wider gap.

The behaviour of the average fast to total charge ratio implies that for the same amount of fast charge, the amount of total charge would be less in the wider gap chamber, resulting in higher ratios. However, this alone does not explain the discrepancy between the obtained values and the theory from **equation 2.11**, which value is around 5%, meaning that we are obtaining lower total charge values than expected.

The culprit of this behaviour has to be the space charge because of the increase in the overall ratio, so that the signals that we are dealing with must correspond to streamers. This makes sense, first of all due to the operating voltages that were used for the measurements and second, due to the capability of detecting a signal without the need of amplifiers of any kind.

4.6 Total Charge

In this section we study the behaviour of the total charge as the voltage applied to the chambers is increased and compare them.

The average for all the total charges for each voltage were taken and plotted. In **Fig. 4.7** we can see the behaviour of the total charge as a function of the voltage. The total charge increases as the voltage increases and, as expected, the narrower gap presents higher average values.

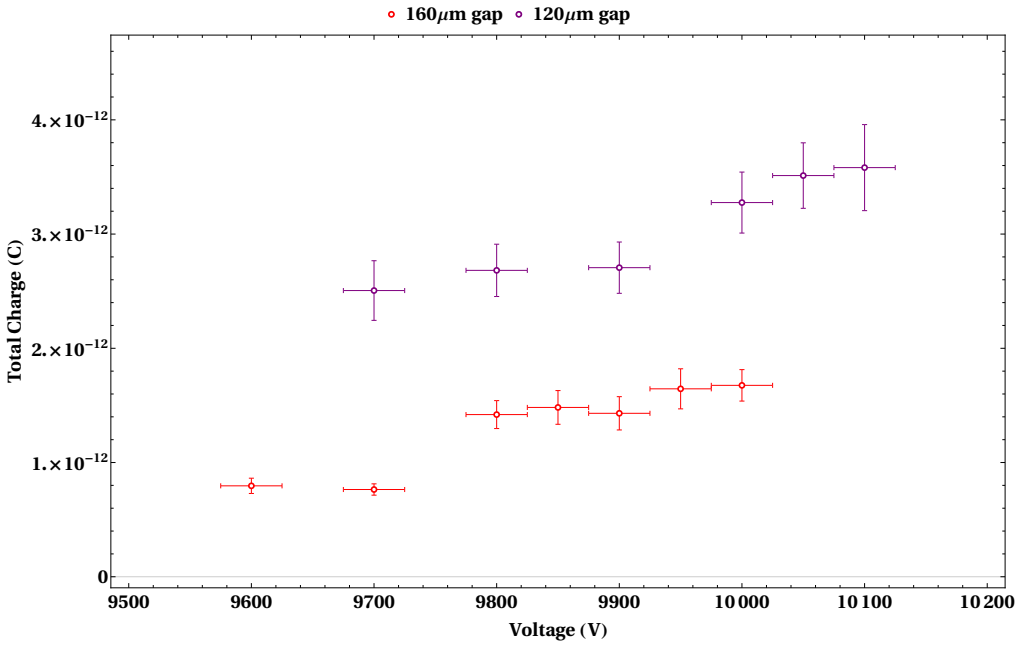

Figure 4.7: Average total charge as a function of voltage for the 120 μm and 160 μm chambers. The voltage shown is the corresponding voltage applied to the anode.

The behaviour again seems to be the same for both chambers, this means that the avalanche process occurs in a similar fashion. However, the values appear to present a flat pattern, contained in a narrow range. This makes sense given the previous results, because as the fast charge increases, the total charge appears to increase but at a much slower pace resulting in an increase of the fast to total ratio.

This unexpected behaviour of the total charge cannot be entirely due to the gas gain, so other effects such as space charge have to be taken into account, mostly due to the very strong electrical fields achieved within the gaps.

4.7 Fast Charge

While it might be redundant to inspect the fast induced charge later as we already examined both the total and the fast to total ratio, interesting or unexpected behaviour can be made more apparent if we analyze it by itself as a function of the increasing voltage.

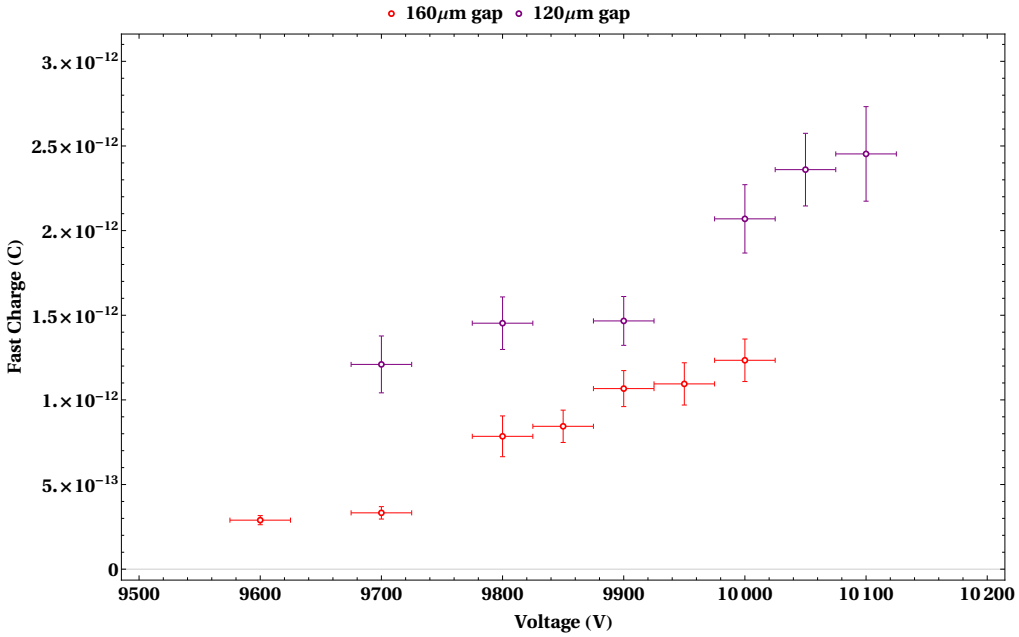

Figure 4.8: Average fast charge as a function of voltage for the 120 μm and 160 μm chambers. The voltage shown is the corresponding voltage applied to the anode.

Comparing **Figures 4.7** and **4.8**, it is clear that both the average fast charge as well as the total charge remain relatively constant until a particular voltage is reached (9800 V for the case of the 160 μm gap, and 10000 V in the case of the 120 μm gap). Since the average fast charge increases faster than the total charge, the fast to total charge ratio increases at these points accordingly. Note that the abrupt increase in slope may characterize a transition and may be related to the avalanche to streamer threshold for the multigap configuration. This is an interesting point meriting further investigation.

Why this transition seems to affect the fast induced charge more, meaning that it affects the appearance of electrons more strongly over other charged particles such as the ions, is the main unknown and will be our principal focus from now onward.

4.8 Streamers

Although we cannot know for sure whether or not a particular event is a real streamer, we can choose a certain condition indicating that a "positive streamer" has taken place. The most reasonable condition makes use of the ratio between the fast and the total induced charge. This takes into account both parts of the avalanche development as they differ from the usual exponential behaviour, something that happens with the formation of streamers.

In **Figures 4.9** and **4.10** the average fast and total charge are shown by taking into account only the positive streamers, which means events with a fast to total ratio larger than or equal to fifty percent. One notes that the overall behaviour is the same as with the inclusion of all events, save for the last data point for the 160 μm chamber, where the statistic might not be as sufficient as the others, resulting in a heavy displacement steeply increasing for the total and heavily decreasing for the fast charge.

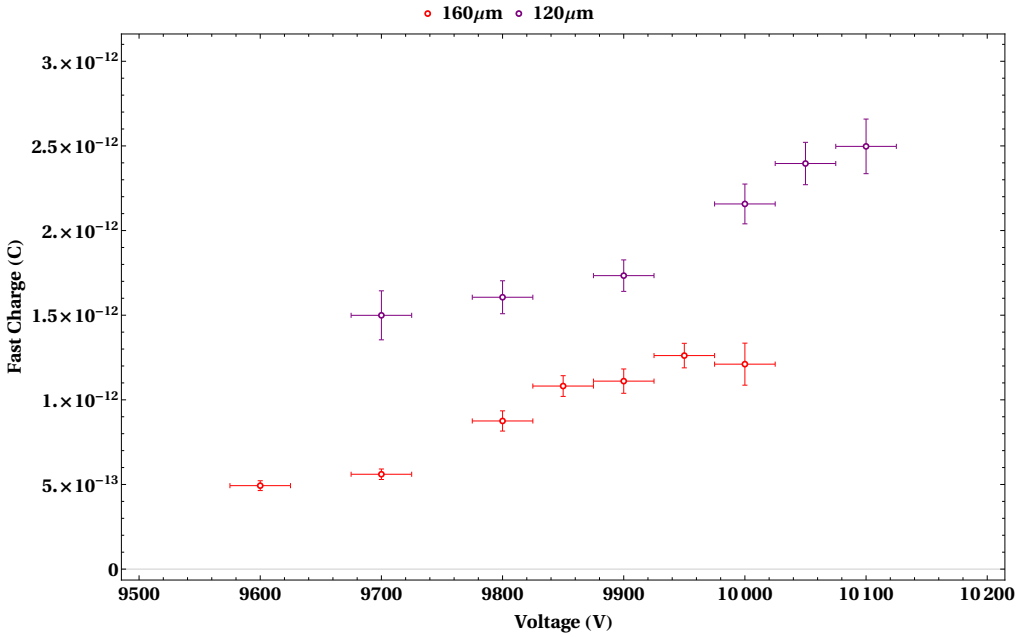

Figure 4.9: Average fast charge of the streamers as a function of voltage for the 120 μm and 160 μm chambers. The voltage shown is the corresponding voltage applied to the anode.

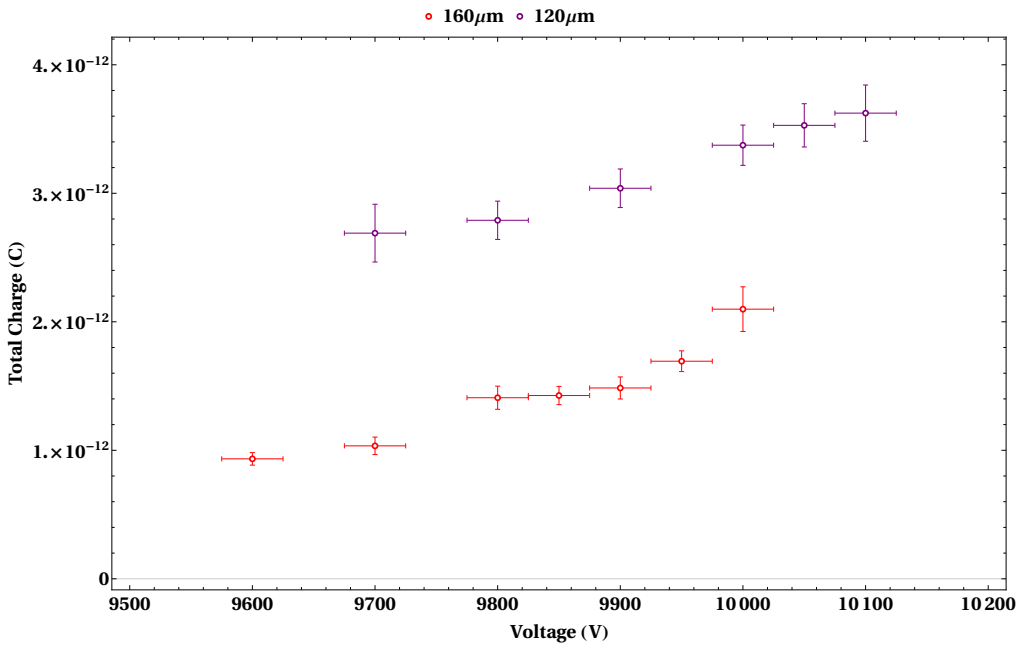

Figure 4.10: Average total charge of the streamers as a function of voltage for the 120 μm and 160 μm chambers. The voltage shown is the corresponding voltage applied to the anode.

There is also a slight increase in the overall amount of charge, more noticeable for the fast charge as we recall from **Figure 4.6**, with the trend showing that as the fast charge increases the ratio also increases resulting in lower total charge. Something that is worth mentioning is that the streamer efficiency increases as the voltage is increased, meaning that the appearance of events whose fast to total ratio is fifty percent or higher tends to increase as the applied voltage rises. This happened to be true for all data points except for the last point (as mentioned above), making it an unfortunate event in an otherwise well-behaved statistic compilation.

The total efficiency of the chambers is depicted in **Figure 4.11** showing that the overall efficiency increases as the voltage does for both chambers. Similar to the efficiency, the streamer appearance increases as the voltage increases. This streamer efficiency, shown in **Figure 4.12**, refers to the probability of events that are considered streamers given that an event was registered. It behaves almost linearly for the most part but this might change with more statistics. We notice that the streamers start to play a more important role as we enter the threshold for the streamer mode of the chambers, this might be at a voltage even higher than the used ones in the experiment, although there is the chance that with more positive streamer events a displacement takes place.

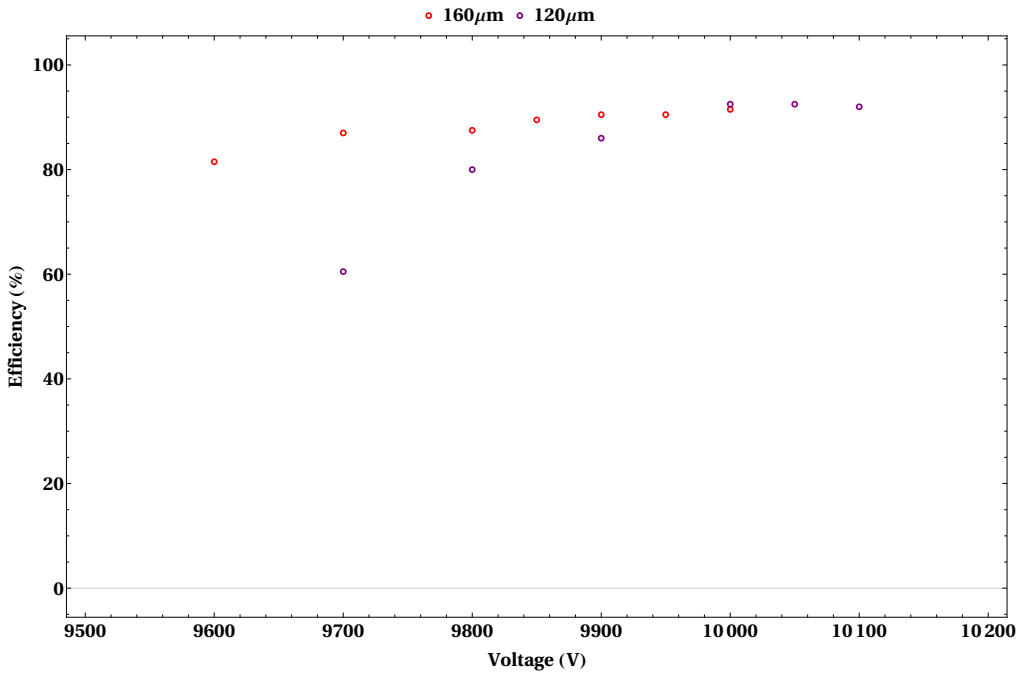

Figure 4.11: Efficiency as a function of voltage for the 120 μm and 160 μm chambers using cosmic rays and no amplification. The voltage shown is the corresponding voltage applied to the anode.

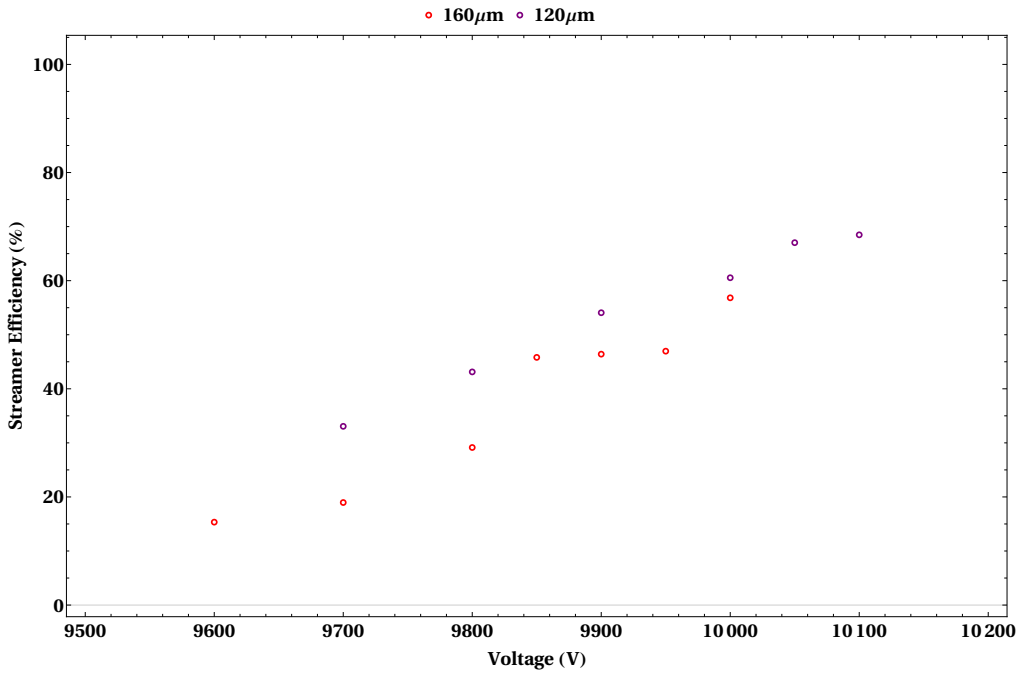

Figure 4.12: Streamer efficiency as a function of voltage for the 120 μm and 160 μm chambers. The voltage shown is the corresponding voltage applied to the anode.

Chapter 5

Parameters for the Simulation of the MRPC

5.1 Voltage and Electrical Field Distribution Inside the Gas Gap

5.1.1 Voltage Distribution

As the designs of the detectors get more and more complicated, the calculation of the electrical field analytically becomes impractical. In order to obtain a numerical solution, simulation software is required. The general design of the double stack MRPC was introduced into **COMSOL** [**11**]. It is set up as a double cathode and a single anode with the appropriate voltages, and solved as a simplified 2D model with the premise that the result also applies for a wide region, near the center of the chamber and away from the borders. We obtained the surface plots for the voltage and the electrical field strength in the perpendicular direction of the chamber.

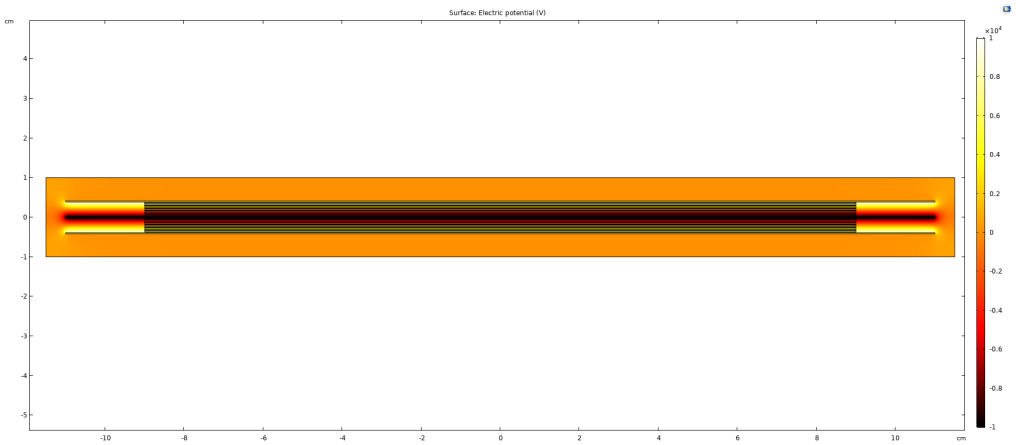

Figure 5.1: Voltage distribution of the MRPC double stack design made via COMSOL.

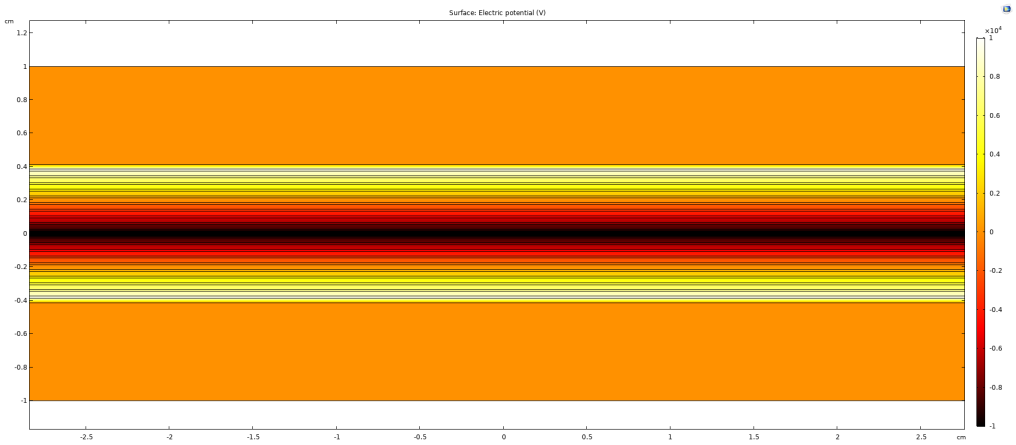

Figure 5.2: Zoom of the gas gaps from the geometry via COMSOL depicting the voltage. The narrow gaps are the gas gaps, while the broader ones are the glass electrodes.

As we can see from the voltage surface plots in **figures 5.1** and **5.2**, the voltage is evenly distributed for each gap, as expected due to the symmetry and equivalence in the design. This means that the voltage for each gap reduces to just the applied voltage divided by the number of gaps. As for the double stack configuration, we note the symmetry of the distribution due to the central anode configuration as it grows towards the external cathodes. We also note the voltage drop outside the chamber due to external grounding.

5.1.2 Electrical field Distribution

For the electrical field strength as shown in **figures 5.3** and **5.4**, the values are equal in magnitude for all the gaps but opposite for different stacks. This agrees with our initial assumption of the electrical field strength, implying that we can use **equation 2.25** in order to obtain these values.

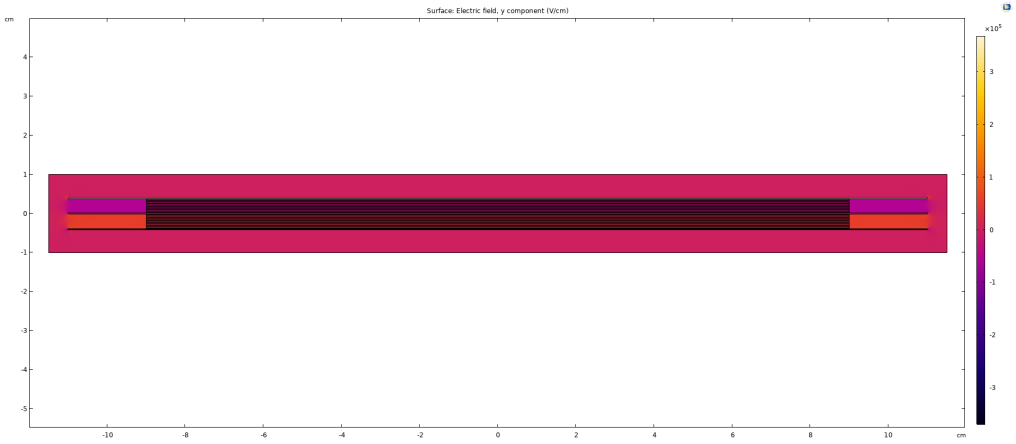

Figure 5.3: Perpendicular component of the electrical field distribution of the MRPC double stack design made via COMSOL.

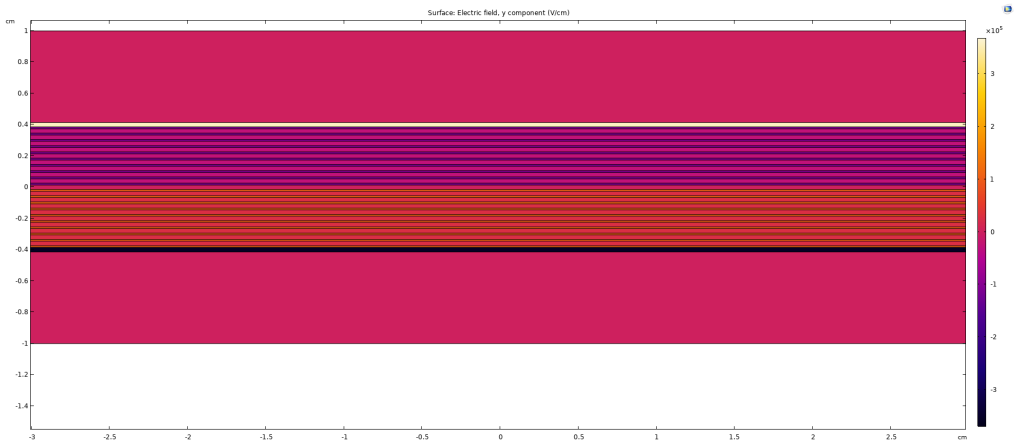

Figure 5.4: Zoom of the gas gaps from the geometry via COMSOL depicting the electrical field. The narrow gaps are the gas gaps while the broader ones are the glass electrodes.

The following table shows the minimum and maximum values of the electrical field tested in our chamber, as well as the comparison with the values obtained using **equation 2.25**:

Gap Size (μm)	Voltage (V)	Simulated E (kV/cm)	Calculated E (kV/cm)
120	9700	137.58	133.18 $\pm$.45
	10100	143.26	138.67$\pm$.45
160	9600	106.07	103.41$\pm$.36
	10000	110.49	107.71 $\pm$.36

Table 5.1: Comparison between calculated and simulated electrical fields. The value of the voltage is the one applied to the anode and the value for ε_r is taken as 12 for the glass in equation 2.25.

The calculated values seem to be around 95% of the values obtained via simulation, serving as a useful approximation to try to calculate phenomena related to the electrical strength applied in the gaps. The good agreement is most likely due to the simple geometry of the detector, not likely for more complicated layouts. However, it is helpful to know that there is an option to obtain a good estimation by means of a simple calculation.

With the information of the electrical strength inside the gap, we can proceed to the next step in the process of understanding signal formation in our chambers.

5.2 Cluster Density

The cluster density is dependent on the gas mixture and the energy of the ionizing particle entering the gap. This value was calculated using **Heed++** via **Garfield++** [**12**], which is a C++ toolkit for the detailed simulation of particle detectors that uses gas and semi-conductors as sensitive medium. The main area of application is currently in micro-pattern gaseous detectors.

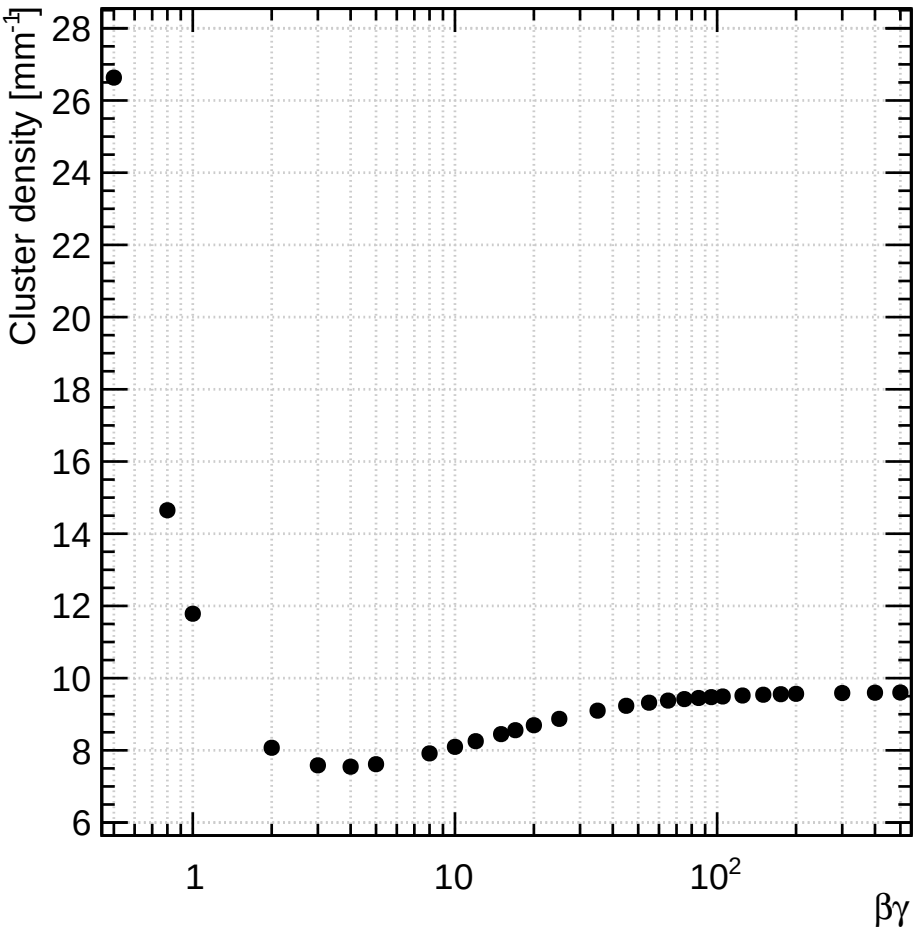

Figure 5.5: Cluster density as a function of the ionizing particle momentum. The gas mixture corresponds to $C_2H_2F_4$ at 95% and SF_6 at 5% .

As can be seen in **Figure 5.5**, $\beta\gamma$ has a value of approximately 5 when the cluster density is at a minimum. It reaches a plateau for higher values, tending to a value of 9 $clusters/mm$. This is the value of interest, due to our use of cosmic rays as triggers for our chambers.

5.3 Energy deposited

Another interesting quantity which can be obtained with the use of Garfield++ is the energy deposited per unit length. This value is dependent on the material composition, the ionizing particle energy and its nature. For example, as neutrons do not have electrical charge, their electromagnetic interaction with the nuclei is almost zero but they can suffer various elastic and inelastic collisions. Water in this case proves to be a fantastic neutron moderator, however this might not be the case with faster neutrons or their decay particles.

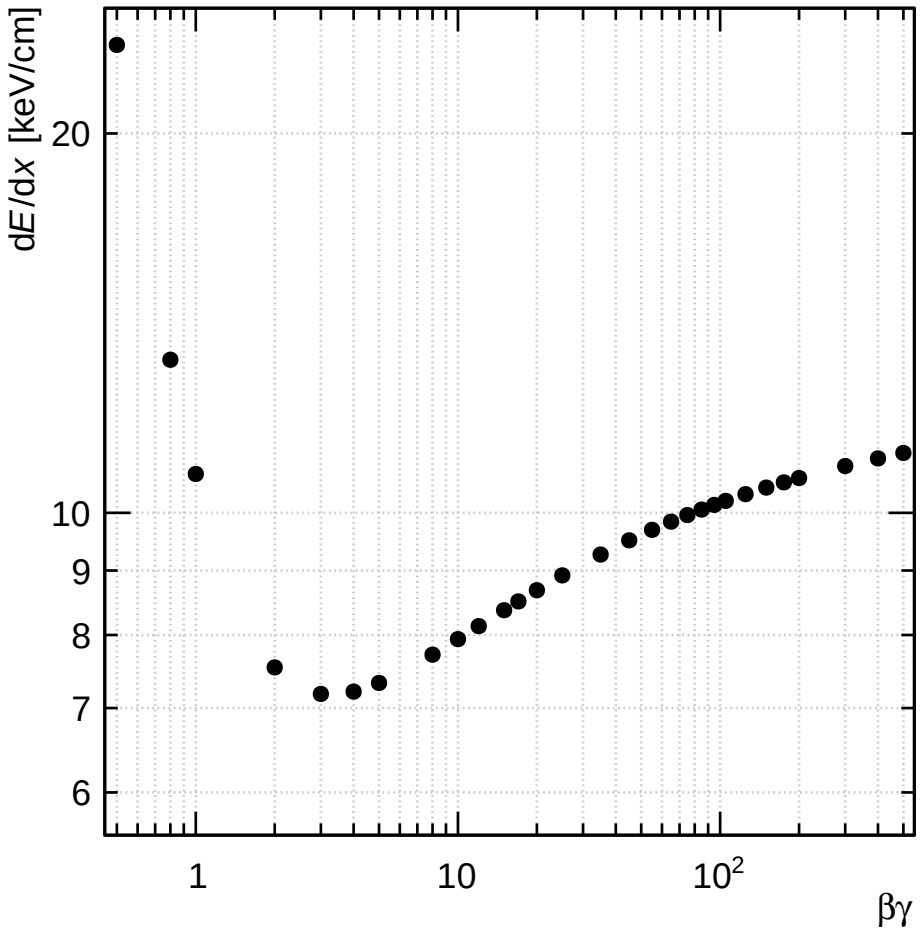

Figure 5.6: Energy deposited as a function of the ionizing particle momentum. The gas mixture corresponds to $C_2H_2F_4$ at 95% and SF_6 at 5%, where the particle was chosen as a muon (μ).

From **Fig. 5.6**, the behaviour of the energy deposited seems to be similar to the cluster density. Nevertheless, the curve rises as the energy increases instead of flattening. Although high, the amount of energy deposited for the same region of cosmic rays is not comparable to its momentum, which means that the ionizing cosmic particles are not fully stopped by the chamber but just pass through. This however, does not take into account all of the other material of the chamber, and would not likely change the

value obtained that much due to its overall thickness.

5.4 Townsend and Attachment Coefficient

Let us assume a single gap of 2mm, filled with our gas mixture and operated in avalanche mode, this means that we use an electrical field that does not allow for a greater gas gain than 10^8, just below the transition from avalanche to streamers. In order to obtain a gain of 10^8 with this size of gap, it will require an effective Townsend coefficient of:

$$e^{\alpha^* * 2mm} \approx 10^8$$

$$\rightarrow \alpha^* * 2mm \approx 8 \ln 10$$

$$\rightarrow \alpha^* \approx \frac{8 \ln 10}{2mm} \approx 9,21 mm^{-1}$$

The value of the fast charge is around 800 fC with the fast to total ratio around 5%.

From **Fig. 5.7**, this value of the field corresponds to an electric field below 60 kV/cm. However, if the gap is reduced (or more realistically the avalanche starts to form in another position such as half the gap width), the gas gain is reduced to an order of 10^5 which reduces the fast signal to 200 aC (a thousand times smaller) making the signal undetectable. This means that only avalanches that start near the cathode, will grow large enough to produce a detectable signal.

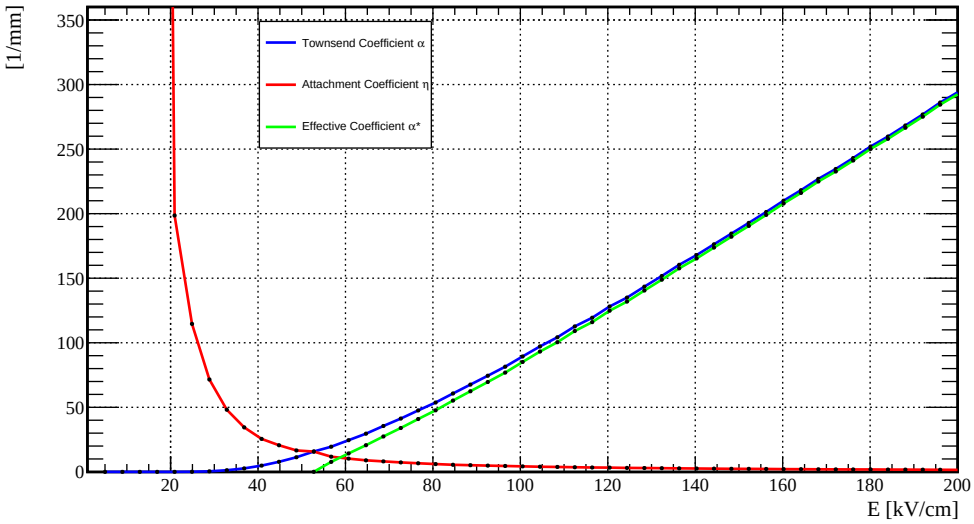

Figure 5.7: Townsend, attachment and effective coefficient for the $C_2H_2F_4$ 95% and SF_6 5% gas mixture as a function of the electrical field strength, via Magboltz simulation.

Fig. 5.7 was computed utilizing **Magboltz** which, like Heed++, is part of the Garfield++ toolkit. It allows one to calculate gas parameters, by solving the Boltzmann transport equations for electrons, in gas mixtures under the influence of electric and magnetic fields.

Gap Size (μm)	E (kV/cm)	Effective coefficient (mm^{-1})
120	137.58	157.008
	143.26	173.196
160	106.07	99.648
	110.49	108.199

Table 5.2: Effective Townsend coefficients obtained via Magboltz for the respective electrical fields.

Following the same reasoning, but taking into account the parameters found previously (such as the cluster density) and using **equation 2.44**, we can calculate the maximum amount of charge induced (for a single 10 gap stack) by the electrons produced by an ionizing particle, with the same conditions as the previous example:

$$Qe_{120\mu m}^{9700V} = .958pC \qquad Qe_{120\mu m}^{10100V} = 6.034pC$$

$$Qe_{160\mu m}^{9600V} = .065pC \qquad Qe_{160\mu m}^{10000V} = .236pC$$

As for the induced charge of the positive ions, the maximum amount that they can induce for a single stack according to **equation 2.46** is:

$$Qi_{120\mu m}^{9700V} = 17.1pC \qquad Qi_{120\mu m}^{10100V} = .112nC$$

$$Qi_{160\mu m}^{9600V} = .977pC \qquad Qi_{160\mu m}^{10000V} = 3.858pC$$

The differences between the two gap configurations are immediately noticeable. The maximum amount of induced charge, that is given by the 160 μm gap, is around 3-5 percent of the charge induced in the 120 μm gap for both electron and positive ions. This is due to the very high gas gain that the narrower gap can achieve. Although the ranges correspond to the values obtained experimentally (especially the order of magnitude), these are too broad to be useful, but they can be used to ascertain the order of magnitude to determine if a configuration can throw a detectable signal.

A more reasonable approach makes use of **equation 2.51**, but without considering the spatial charge corrections. Taking into account only the saturated charge to obtain a range for which the calculated induced charge corresponds to the experimental value, we then use the correction to the spatial charge to understand how this affects the calculations.

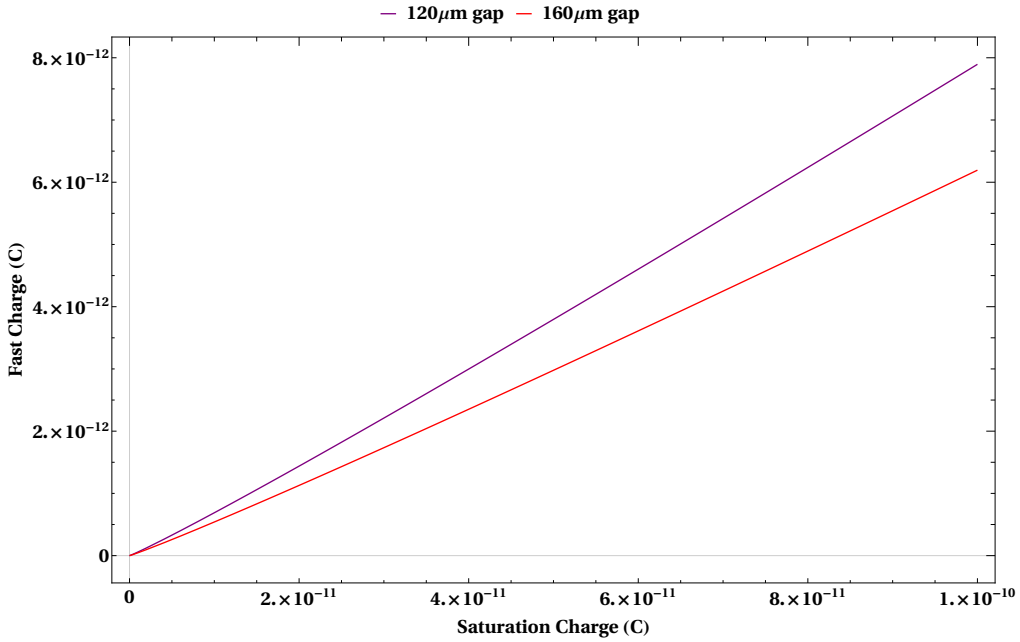

Figure 5.8: Comparison of the increase of the induced charge as a function of the charge saturation for both gap size configurations.

The differences shown in **Figure 5.8** are noteworthy. The slope of the line that corresponds to the narrower gap chamber is steeper, as it should be. This is due to the fact that, for the same amount of charge inside the gap, the charge density will be larger for the narrower gap. The range of the fast charge is more reasonable compared to those obtained in the previous calculation using **equation 2.44**. Because of this, we will use this behaviour of the charge in our simulation to compare with experimental results. We will also improve them using spatial charge corrections.

5.5 Drift Velocity

The drift velocity, refers to the velocity at which the charged particles are carried towards the electrodes, due to the electrical field present inside the gap. As we noted above, the signal is dependent on this drift of the charged particles, which in turn are also dependent on the gas gain, which depends on the electrical field and so on.

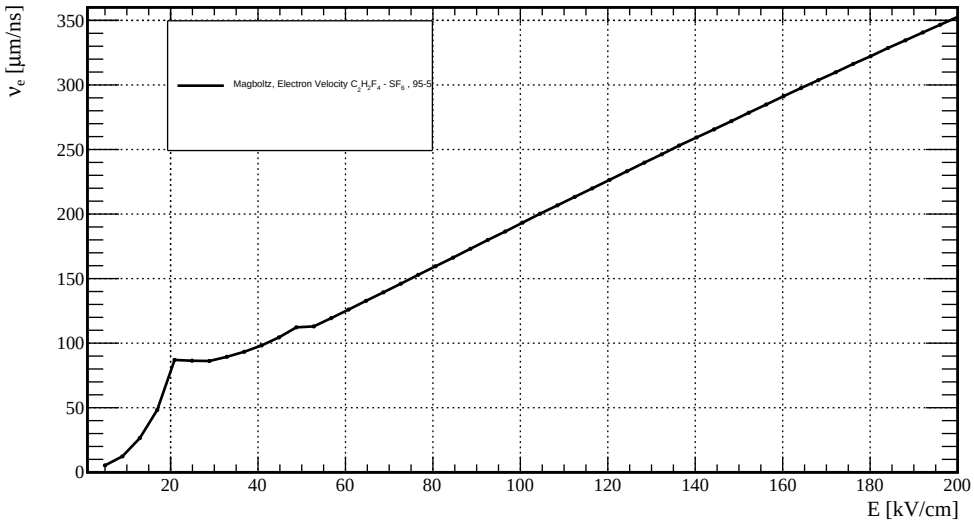

Figure 5.9: Electron drift velocity for the $C_2H_2F_4$ 95% and SF_6 5% gas mixture as a function of the electrical field strength via Magboltz simulation.

In **Figure 5.9** the drift velocity of the electrons in our gas mixture is depicted. At lower electrical field strengths its behaviour is exponential, but as the electrical field gets stronger it presents a linear behaviour. This is perhaps directly related to the same behaviour of the induced charge as space charge effects manifest.

This data is another parameter, which will play an important role in our final simulation of the MRPC, to try to retrieve information about the induced charge. The comparison with experimental data will tell us how good our toy model is.

5.6 Diffusion

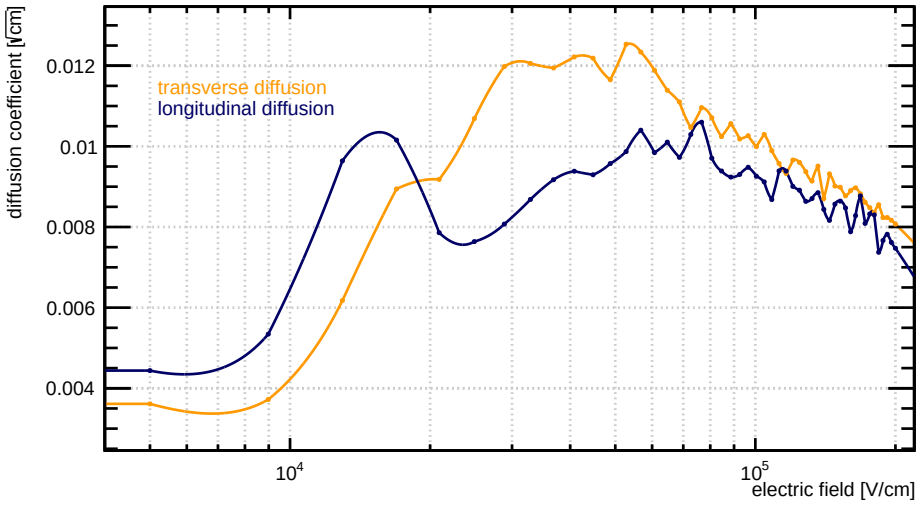

Figure 5.10: Electron longitudinal and transverse diffusion (for the $C_2H_2F_4$ 95% and SF_6 5% gas mixture) as a function of the electrical field strength, via Magboltz simulation.

The transverse and longitudinal diffusion are depicted in **Figure 5.10**, which basically shows the propagation of the electron cloud, both perpendicularly as well as parallel. These values are also affected in the simulation, by a randomized factor, that tries to emulate the stochastic nature of the avalanche growth.

The simulation is for the most part 1-dimensional, taking into account longitudinal diffusion. However, transverse diffusion is also taken into account to calculate the electron cloud growth, making it an almost 1.5-dimensional simulation. This is not the only exception for the dimension of the simulation: the calculation of the space charge also takes into account a radius around the charges, that strongly affects avalanche development.

Now that we have all the information for the necessary parameters, the next step is to implement them in a simulation. This will help us to obtain information on how this affects the charges, as the avalanche evolves into a streamer, and how this affects the induced signal retrieved.

Chapter 6

Description of the MRPC Simulation

The Multi Gap Resistive Plate Chamber is simulated simply as the collection of gas gaps contained within it. This is achieved via the *Garfield++* framework, which implements the aforementioned *Magboltz* simulation for the gas transport parameters, and *Heed++* for the ionization. A high electrical field is applied across the gas gaps. A single muon μ of around 5 GeV is shot at the center of the gas gaps producing ionization along its path. An avalanche is then produced and the signal that the drifting charges generates is computed.

The physical processes that take place inside the gaps are calculated as the avalanche grows. This is taken for the most part as a 1-dimensional process for computing efficiency, taking into account a radius around the charges in order to obtain the space charge effects and diffusion of the electrons. The gas gap is divided in a number of steps to make the calculation process easier and to be able to reevaluate each important parameter and physical process in each step.

The simulation is based in the work of Vincent Français in **[6]**, mostly in the way that approximates how the electronic avalanche itself evolves. Its simulation consists of a single Resistive Plate Chamber gap, that works at low electrical fields not higher than 60 keV/cm. Our simulation is a simplified version of the Avalanche code but applied to a Multi Gap, with the simplifications allowing us to work at higher electrical fields overall. The cost of these simplifications are explained later in the chapter as they limit the usefulness of the code and the data retrieved with it.

6.1 Simulation Algorithm

The process of the simulation can be summarized as follows:

1. The gap is separated in length steps where the physical process is calculated. This reduces simulation time without compromising the results too much. The length of these steps is given by $\frac{g}{N}$, where g is the gap width and N an integer. This implies that the corresponding time steps are given by $\frac{g}{v_0}$ where v_0 is the initial drift velocity of the electrons.

2. A single muon μ is shot at the gas gaps producing ionization along its path, which is calculated with *Heed++*. A cluster is produced and the avalanche initialized. The initial gas parameters were previously calculated with *Magboltz*.

3. The space charge is computed at each step, affecting the electrical field. The effective Townsend coefficient $\alpha - \eta$, the drift velocity and other relevant parameters are then calculated in order to obtain the production of the electrons in the next step. The signal and induced charge are similarly calculated.

4. The process of electron multiplication is repeated until all the electrons reach the anode or are captured. The data is finally written into files for later analysis.

6.2 Limitations of the Simulation

One of the main limitations of this simulation is the amount of charges that are able to be present at a certain step, with a current limit of roughly 10^9 electrons, conditions which mostly occur at high electrical fields. For this reason the simulation is cut as soon as it reaches this threshold in order to avoid soft-locking. This can be prevented for calculations, by using lower electrical fields, avoiding the streamer mode. Nevertheless the experiment was run in streamer mode, making this problem noticeable. Luckily, the electron production linearizes in this case, so that the simulation is still useful in obtaining the slope of this line, which is later used as a workaround. The simulation time when this happens is around 10 ns, where the next 20 ns can be obtained by calculations. This is not optimal but allows for comparison with experiment.

Another limitation of this simulation is the lack of a photo ionization model of the gases, most notably SF_6, which are important for the avalanche to streamer transition. The transition affects the gas density by producing ions and separating them into different compounds. There is no workaround for this problem. As such, a model will need to be implemented to improve the quality of the data acquired.

Chapter 7

Simulation Results

As stated before, the simulation is unfortunately unable to go higher than 10^9 electron charges. This is due to a soft-lock that occurs in the next step of the calculation, which takes too long to complete. The workaround is shown in **Figure 7.1** and **Figure 7.2** for the fast and total charges. This workaround applies a linear approximation as the space charge regime takes place. This usually happens during the first 10 ns of the simulation, requiring additional manual calculations in order to compare with experimental results.

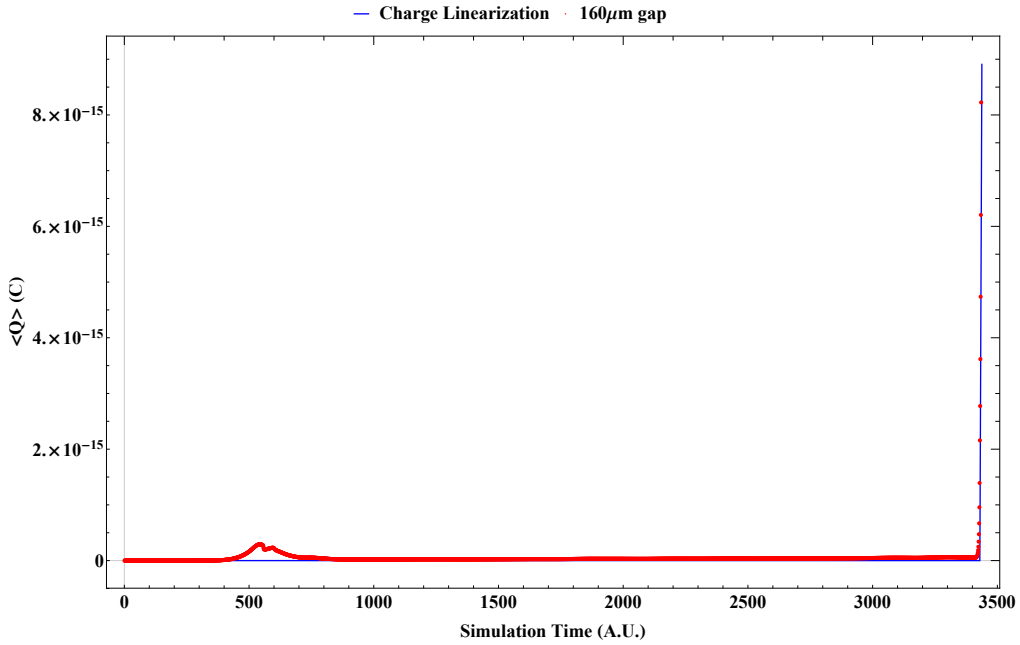

Figure 7.1: Simulation of an electron avalanche, in the 160 μm gap configuration, compared to the linearization of the charge as a streamer forms. The avalanche can be seen in the left part of the graph and the streamer in the right.

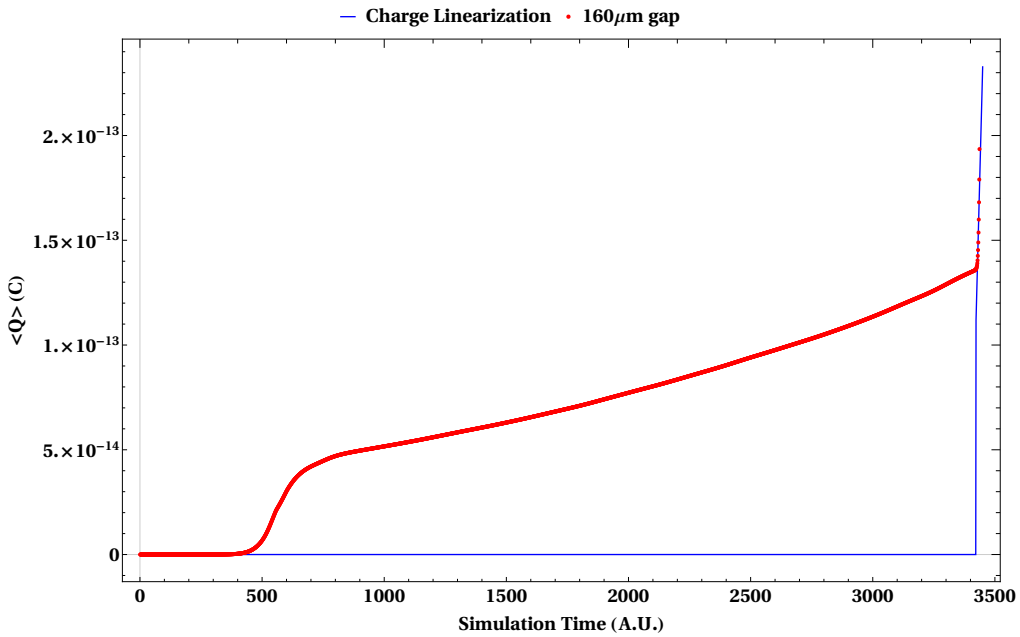

Figure 7.2: Simulation of an avalanche, in the 160 μm gap configuration, compared to the linearization of the total charge as a streamer forms.

In **Figure 7.3** the random nature of the events, translated in various slopes for the charge linearization, is shown. The range of the average fast charge seems to be almost 10 times higher than expected. However, by using **equation 2.51**, these values can be filtered as the raw "saturation charge" to finally obtain the induced charge.

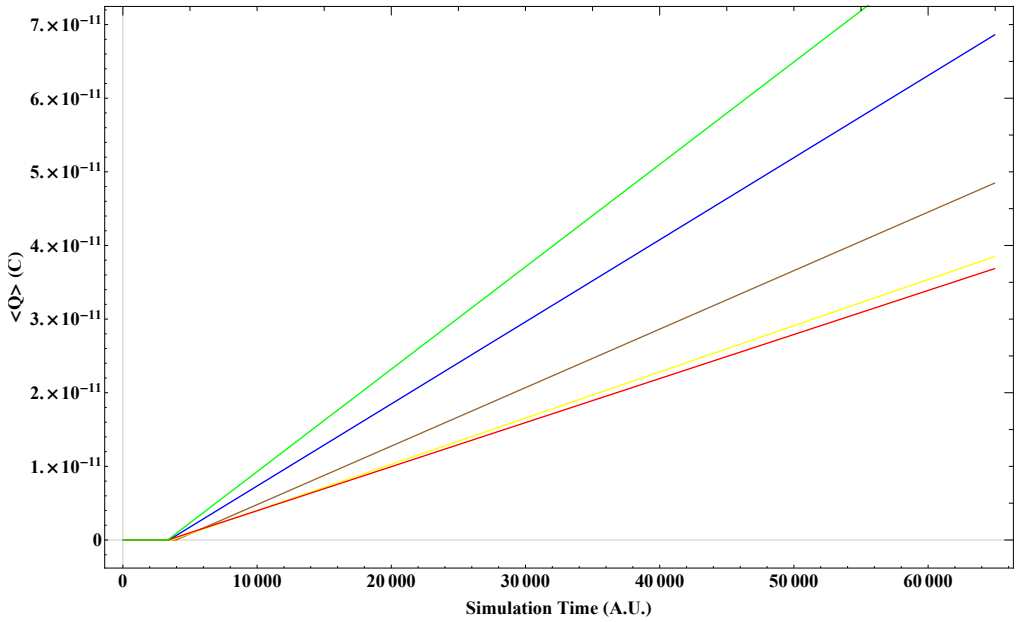

Figure 7.3: Linearization of the fast charge for different events. The simulation time corresponds to the first 100 ns. This still corresponds to the "saturation charge", so a latter correction still needs to be applied. The same applies to the total charge.

The implementation of this idea is depicted in **Figure 7.4** and **7.5** for the fast and total induced charge, where the charge is now a function of the simulation time and the position of the charges. The ranges seem to be more reasonable than the ones without filtering, so we decided to stick with this simple approach. The time taken was 30 ns which, as can be appreciated in **Figure 4.5**, is the time that it takes the fast signal to finish.

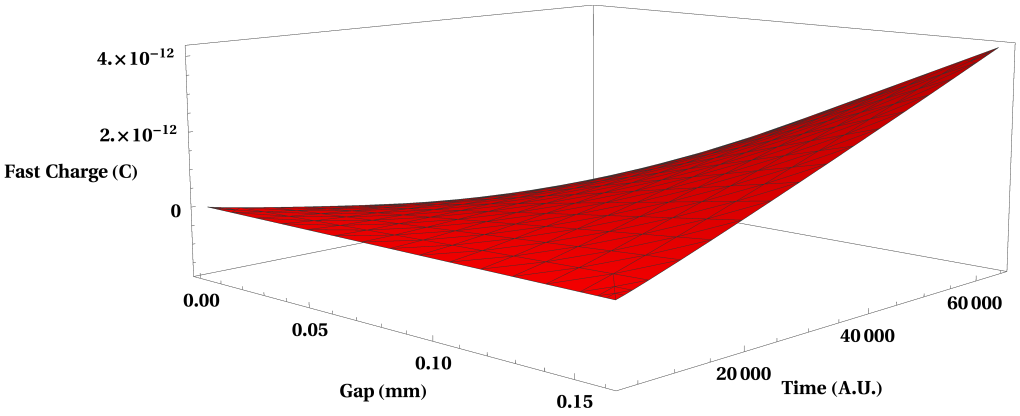

Figure 7.4: Induced fast charge as a function of the simulation time and the distance. The simulation time corresponds to the first 100 ns.

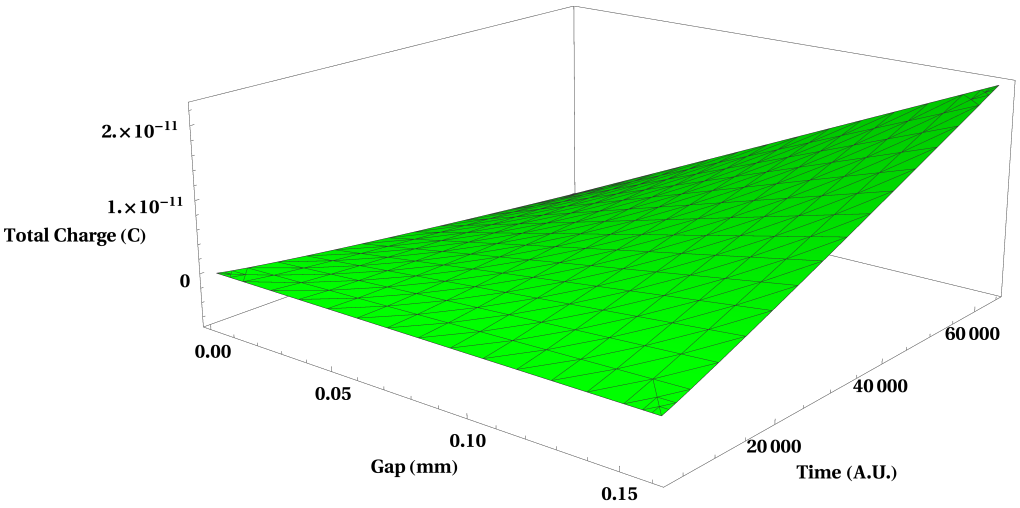

Figure 7.5: Induced total charge as a function of the simulation time and the distance. The simulation time corresponds to the first 100 ns.

The resulting average charge is shown in **Figs. 7.6** and **7.7**. The problems of the approach are immediately apparent, but let us first consider its uses. The calculations can be useful as a rough estimate for the amount of charge, that a chamber working in streamer mode will be subjected to. The thresholds so obtained, can also be used in the estimation of new designs, whose gap widths are between the ones that were utilized.

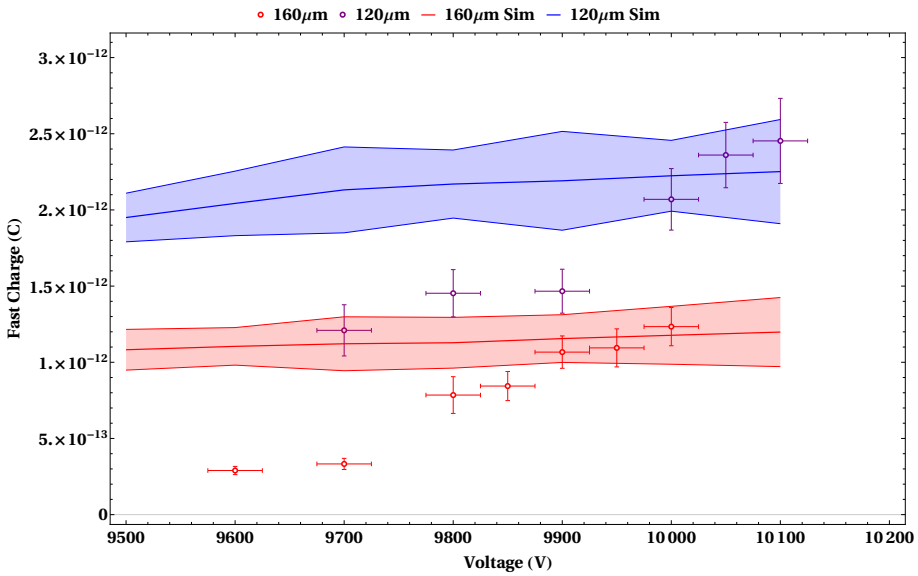

Figure 7.6: Average experimental fast charge compared with the simulated one, for both chambers, as a function of the voltage. The top part of the band corresponds to the charge evaluated at the total gap width. The lower part of the band has been taken at 75% of this value, as this is the lower bound allowing for a retrievable signal.

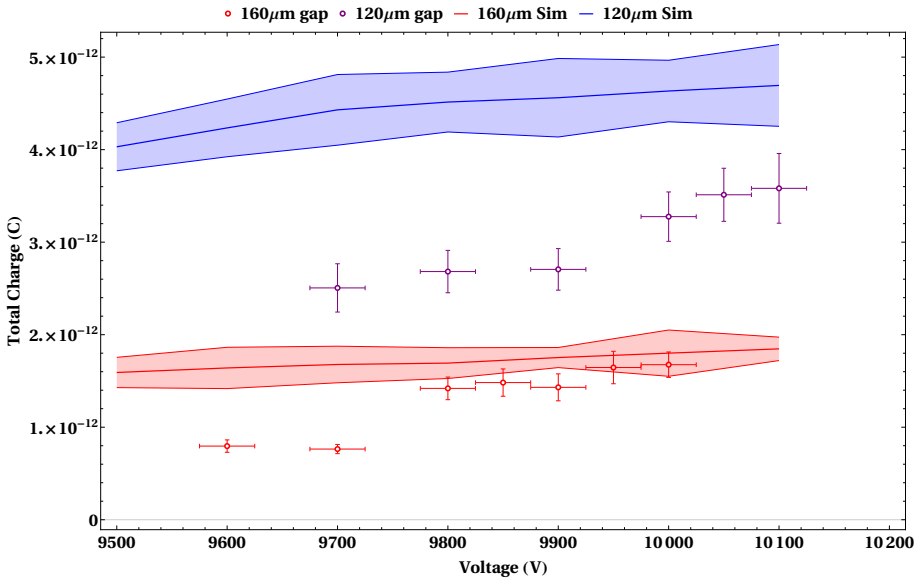

Figure 7.7: Average experimental total charge comparison with the simulated one, for both chambers, as a function of the voltage. The top part of the band corresponds to the charge evaluated at the total gap width. The lower part of the band has been taken at 75% of this value, as this is the lower bound allowing for a retrievable signal.

Although the approach is simple in that it just fits a linear growth model to avalanche development, it requires an event by event analysis, making the necessary statistics a complicated process. Nevertheless, doing the calculation for a couple of points to ob-

tain a range of the charge is valuable. Due to the limitations of the simulation, such as soft locks when the amount of charges increases or the lack of photo ionization, the results differ in quantity and behaviour from experiment. However, as the order of magnitude is comparable, this allows for retrieval of the signal without the use of an amplifier beforehand, which is useful for new designs working in streamer mode.

The fast to total ratio obtained by the simulation, is always around fifty percent for the 120 μm gap and seventy percent for the 160 μm gap. This means that, according to our streamer definition, the average event for the simulation is considered a streamer. It is also considered a streamer due to the fact that most events surpass the gas gain threshold or Raether limit. However, the largest increment as the voltage increases occurs for the total charge, contradicting the experimental results and causing the fast to total ratio to decrease. Perhaps, by using higher voltages in the simulation one can also increase the fast to total ratio, but it seems from the results obtained here that, without the implementation of an extra model to take into account the experimental behaviour, the increment might be unlikely.

Chapter 8

Conclusions

The Multigap Resistive Plate Chamber has proven to be a very complex detector. Although very simple in design, it undergoes a series of complicated physical processes that makes the prediction of the results interesting.

The difference in the charge produced by both chambers is considerable for a minimal change in the design. Furthermore, considering that it normally is used under extreme radiation, such as radioactive sources, these differences will be even more noticeable. However, the use of chambers in streamer mode, staying at high voltages, is not advisable due to the low efficiency at higher rates. The main reason for us to work in streamer mode was the lack of an available amplifier at the moment.

The largest unknown is the rapid increase in the fast charge compared to the total charge, resulting in steep growth for the fast to total ratio. The simulation achieved a fast to total ratio around fifty percent, although the pattern was remarkably flat. This likely means that many vital processes in the streamer formation are lacking or missing, such as photoionization, which are important in the avalanche to streamer transition. This is another department where a simple model could make an improvement to see if any changes occur.

The simulation of the Multigap Resistive Plate Chamber proved to be rather difficult. Many improvements to the simulation can be attempted, such as allowing for a distribution in the muon momenta instead of just a mono-energetic one, changing the electron charge distribution to a simpler one in order to improve simulation time and possibly increasing the amount of in-simulation time that can be achieved. We could also change the fit to a more accurate function of the charge. However, these changes take time and may not work at all, and so are planned to be implemented later.

The simulation is not capable of finishing a complete streamer development. However, it is capable of simulating complete avalanche growth. By reducing the operating voltage, the simulation would be capable of retrieving a signal from avalanches, making it possible to compare the results with avalanche mode. Although, in order to obtain a signal from these avalanches experimentally, the use of an amplifier is mandatory due to the charge being various orders of magnitude lower in the case of avalanches.

Chapter 9

Bibliography

[1] Cub, J., C. Gund, D. Pansegrau, G. Schrieder, and H. Stelzer: *A position sensitive parallel plate avalanche counter for single particle and current readout.* Nuclear Instruments and Methods in Physics Research Section A: Accelerators, Spectrometers, Detectors and Associated Equipment, 453(3):522–524, Oct 2000. http://dx.doi.org/10.1016/S0168-9002(00)00461-7.

[2] Raether, H.: *Electron Avalanches and Breakdown in Gases.* Butterworths advanced physics series. Butterworths, 1964. https://books.google.com.mx/books?id=2nSCvEq6AFcC.

[3] Yasar Onel, Burak Bilki: *Digital calorimetry for fcc detectors*, 2019. https://slideplayer.com/slide/13438182/.

[4] Peskov, Vladimir, Marcello Abbrescia, and Paulo Fonte: *Resistive Gaseous Detectors Designs, Performance, Perspectives.* Wiley-VCH, 2018.

[5] Garcia, Alejandro Laso: *Timing Resistive Plate Chambers with Ceramic Electrodes: for Particle and Nuclear Physics Experiments.* PhD thesis, Dresden, Tech. U., Dept. Math., 2014.

[6] Français, Vincent: *Description and simulation of the physics of resistive plate chambers.* Nuclear Experiment [nucl-ex]. Université Clermont Auvergne. English. NNT : 2017CLFAC035. tel- 01727712, 2017.

[7] He, Zhong: *Review of the shockley–ramo theorem and its application in semiconductor gamma-ray detectors.* Nuclear Instruments and Methods in Physics Research Section A: Accelerators, Spectrometers, Detectors and Associated Equipment, 463(1–2):250–267, May 2001. http://dx.doi.org/10.1016/S0168-9002(01)00223-6.

[8] Fonte, P: *Survey of physical modelling in resistive plate chambers.* Journal of Instrumentation, 8(11):P11001–P11001, Nov 2013. http://dx.doi.org/10.1088/1748-0221/8/11/P11001.

[9] Lippmann, Christian and Werner Riegler: *Space charge effects in resistive plate chambers.* Nuclear Instruments and Methods in Physics Research Section A: Accelerators, Spectrometers, Detectors and Associated Equipment, 517(1–3):54–76, Jan 2004. http://dx.doi.org/10.1016/j.nima.2003.08.174.

[10] Liu, Z., F. Carnesecchi, M.C.S. Williams, A. Zichichi, and R. Zuyeuski: *Timing performance study of multigap resistive plate chamber with different gap size.* Nuclear Instruments and Methods in Physics Research Section A: Accelerators, Spectrometers, Detectors and Associated Equipment, 927:396–400, May 2019. http://dx.doi.org/10.1016/j.nima.2019.02.068.

[11] COMSOL: *software.* https://www.comsol.com/.

[12] Garfield++: *framework.* https://garfieldpp.web.cern.ch/garfieldpp/.

[13] Akindinov, A.N., A. Alici, F. Anselmo, P. Antonioli, Y. Baek, M. Basile, G. Cara Romeo, L. Cifarelli, F. Cindolo, F. Cosenza, and et al.: *Space charge limited avalanche growth in multigap resistive plate chambers.* The European Physical Journal C, 34(S1):s325–s331, Jul 2004. http://dx.doi.org/10.1140/epjcd/s2004-04-031-9.

[14] Akindinov, A.N., A. Alici, P. Antonioli, S. Arcelli, M. Basile, G. Cara Romeo, L. Cifarelli, F. Cindolo, A. De Caro, S. De Pasquale, and et al.: *Operation of the multigap resistive plate chamber using a gas mixture free of flammable components.* Nuclear Instruments and Methods in Physics Research Section A: Accelerators, Spectrometers, Detectors and Associated Equipment, 532(3):562–565, Oct 2004. http://dx.doi.org/10.1016/j.nima.2004.04.249.

[15] Bromley, Jane T: *Investigation of the Operation of Resistive Plate Chambers.* Master's thesis, Manchester U., 1994.

[16] Riegler, Werner, Christian Lippmann, and Rob Veenhof: *Detector physics and simulation of resistive plate chambers.* Nuclear Instruments and Methods in Physics Research Section A: Accelerators, Spectrometers, Detectors and Associated Equipment, 500(1–3):144–162, Mar 2003. http://dx.doi.org/10.1016/S0168-9002(03)00337-1.

[17] Riegler, Werner and Christian Lippmann: *The physics of resistive plate chambers.* Nuclear Instruments and Methods in Physics Research Section A: Accelerators, Spectrometers, Detectors and Associated Equipment, 518(1–2):86–90, Feb 2004. http://dx.doi.org/10.1016/j.nima.2003.10.031.